AIMS Mathematics, 11(4): 11948–11976.
DOI: 10.3934/math.2026490
Received: 18 February 2026
Revised: 08 April 2026
Accepted: 15 April 2026
Published: 28 April 2026

https://www.aimspress.com/journal/Math

Research article

Incremental harmonic balance method based on asymptotic expansion and a trust-region strategy and application to strongly nonlinear systems

Wentao Zhou[1,2], Zeliang Liu[1,2]* and Huijian Li[1,2]

[1] School of Civil Engineering and Mechanics, Yanshan University, Qinhuangdao 066004, China
[2] Hebei Key Laboratory of Mechanical Reliability for Heavy Equipments and Large Structures, Yanshan University, Qinhuangdao 066004, China

* **Correspondence:** Email: liuzeliang@ysu.edu.cn.

Abstract: To address the narrow convergence basin and high sensitivity to initial guesses of the incremental harmonic balance method in the analysis of strongly nonlinear systems, this paper develops an enhanced approach that combines a trust region strategy with asymptotic expansion. In each incremental step, an artificial asymptotic parameter is introduced, and the nonlinear incremental equations are expanded into a series of linear recursive subproblems based on the Hessian matrix, enabling order-by-order decoupling of the response components. Furthermore, a trust region algorithm is employed as the inner solver to adaptively control the iteration step size, ensuring robustness and global convergence in solving each subproblem at each order. Numerical examples demonstrate that the proposed method preserves the accuracy of the traditional approach, while significantly widening the convergence basin, reducing dependence on initial guesses, and tracing the frequency response curve with fewer iterations and less computational time. The method, therefore, provides a semi-analytical framework with robust convergence and high computational efficiency for periodic response analysis of strongly nonlinear systems.

Keywords: incremental harmonic balance method; trust-region algorithm; asymptotic expansion; strongly nonlinear systems; Hessian matrix; periodic solutions
Mathematics Subject Classification: 37M05, 37M15

1. Introduction

Nonlinear dynamical phenomena are ubiquitous in a wide range of engineering systems, and accurate computation and stability analysis of their periodic responses are of substantial theoretical and practical importance [1–3]. In traditional analytical methods such as the Lindstedt–Poincaré method [4,5], the method of multiple scales [6,7], and averaging [8,9], derivations are often cumbersome and are typically limited to weakly nonlinear systems. Purely numerical approaches, including the Runge–Kutta method [10,11], the finite element method [12,13], and the boundary element method [14], can handle strongly nonlinear problems; however, they are often inefficient for systematic parametric studies, tracking multiple solution branches, and computing unstable solutions, and are sensitive to initial conditions. To combine the insight of analytical methods with the generality of numerical methods, Lau and Cheung [15] proposed the incremental harmonic balance (IHB) method. This method is a semi-analytical and semi-numerical approach based on the Galerkin procedure and Newton–Raphson iterations. By incremental linearization and frequency-domain balancing, it can compute periodic responses of strongly nonlinear systems, and their stability can be analyzed via Floquet theory [16]. To date, the IHB method has been widely applied in vehicle engineering [17,18], civil engineering [19,20], aerospace engineering [21,22], and other fields.

Despite its broad applicability, two intrinsic bottlenecks still constrain the performance of the IHB method in complex, strongly nonlinear systems. First, computational efficiency remains to be improved. In classical IHB, the system matrix must be fully reconstructed at each Newton iteration, which is costly for multi-degree-of-freedom problems or parameter sweeps. Considerable efforts have therefore been devoted to developing efficient algorithms: Lu et al. [23] optimized the Galerkin procedure using the fast Fourier transform (FFT); Zhu [24] and co-workers combined Broyden's method with FFT to accelerate the computation of the residual and Jacobian; and Ju et al. [25] introduced tensor contraction techniques. For complex structures with large-scale degrees of freedom, Hui et al. [26] proposed a decoupling strategy in which IHB is applied only to the nonlinear components, significantly reducing the computational scale. Chen et al. [27,28] employed dimension reduction and FFT to accelerate Jacobian computation for high-dimensional sparse nonlinear systems and introduced automatic differentiation into the harmonic balance framework, thereby eliminating manual derivation and enabling the handling of arbitrary nonlinearities. Second, convergence robustness urgently needs enhancement. The convergence of IHB strongly depends on the initial guess. For strongly nonlinear, nonsmooth, or dynamically complex systems (e.g., self-excitation, hysteresis, internal resonance), the method may diverge or converge to nonphysical solutions. To address convergence issues, Chen and Liu [29] combined homotopy analysis with IHB to broaden the basin of convergence; Zheng et al. [30] introduced Tikhonov regularization to treat ill-conditioned equations; Li et al. [31] employed the Levenberg–Marquardt algorithm to enhance iterative stability. Dai et al. [32,33] proposed the reconstruction harmonic balance method, which solves the symbolic explosion problem of high-order harmonic balance. Subsequently, they combined RHB with recasting techniques and extended it to non-polynomial nonlinear systems and quasi-periodic response calculations. Notably, integrating optimization algorithms (e.g., backtracking line search [34] and trust-region methods [35]) with IHB to improve convergence robustness and leveraging higher-order tensor information (e.g., Hessians) [36] to improve iteration performance have become important research directions in recent years.

Existing improvements have demonstrated various advantages (e.g., high accuracy [27,28] and symbolic handling [32,33]; convergence stability [35]), while the proposed TRE-IHB method targets a different need: broadening the convergence basin and reducing sensitivity to initial guesses. To this end, this paper proposes an enhanced incremental harmonic balance method that integrates asymptotic expansion with a trust-region strategy (TRE-IHB). The main contributions are as follows: (1) a serialized decoupling framework that expands the nonlinear incremental equations into a sequence of linear subproblems using the Hessian matrix, yielding a smoother iteration path; (2) a trust-region dogleg solver with a jump–backtracking mechanism that ensures global convergence, reduces dependence on initial guesses, and helps escape local minima; and (3) systematic comparisons with traditional IHB and TR-IHB, demonstrating that TRE-IHB significantly broadens the convergence basin while maintaining accuracy and reducing computational cost.

The remainder of this paper is organized as follows: Section 2 presents the proposed TRE-IHB method in detail, including the incremental–asymptotic expansion procedure, the harmonic balance formulation, and the integration with the trust-region dogleg solver. Section 3 describes the stability analysis of periodic solutions based on Floquet theory and the adaptive arc-length continuation strategy for tracing frequency–response curves. In Section 4, three representative strongly nonlinear systems are investigated to validate the accuracy, robustness, and efficiency of the proposed method. Finally, the paper concludes with a summary of key findings and an outlook on future work.

2. Methodology for periodic responses

Consider a general strongly nonlinear vibration system, whose equation of motion can be written as

$$\boldsymbol{M}\frac{d^2\boldsymbol{q}}{dt^2}+\boldsymbol{C}\frac{d\boldsymbol{q}}{dt}+\boldsymbol{K}\boldsymbol{q}+\boldsymbol{G}(\boldsymbol{q})=\boldsymbol{F}\cos(m\omega t), \tag{1}$$

where $\boldsymbol{q}=[q_1,q_2,\ldots\ldots q_n]^T$ is the system displacement vector; $\boldsymbol{M}$, $\boldsymbol{C}$ and $\boldsymbol{K}$ are the mass, damping, and linear stiffness matrices of the system, respectively; $\mathbf{G}(\boldsymbol{q})$ is the nonlinear force vector; $\boldsymbol{F}$ is the excitation vector; m is the harmonic order of excitation; and ω is the excitation frequency.

Introduce the time-scale transformation $\tau=\omega t$. Equation (1) can be rewritten as

$$\omega^2\boldsymbol{M}\frac{d^2\boldsymbol{q}}{d\tau^2}+\omega\boldsymbol{C}\frac{d\boldsymbol{q}}{d\tau}+\boldsymbol{K}\boldsymbol{q}+\boldsymbol{G}(\boldsymbol{q})=\boldsymbol{F}\cos(m\tau), \tag{2}$$

where $\boldsymbol{q}(\tau)=\boldsymbol{q}(t)$, and the periodicity condition $\boldsymbol{q}(\tau+2\pi)=\boldsymbol{q}(\tau)$ holds.

2.1. Incremental–asymptotic expansion procedure

The first step of TRE-IHB is the incremental-asymptotic expansion procedure. Let $\boldsymbol{q}_0$ and ω_0 denote the initial solution of Eq (2). Its neighborhood can be expressed in the incremental form as

$$\boldsymbol{q}=\boldsymbol{q}_0+\Delta q,\omega=\omega_0+\Delta\omega. \tag{3}$$

By jointly considering Eqs (2) and (3) and performing a Taylor expansion at $(q_0,\ \omega_0)$ while retaining terms up to second order, the quadratic nonlinear incremental equation in matrix form is obtained:

$$\underbrace{\omega_0^2\boldsymbol{M}\frac{d^2\Delta\boldsymbol{q}}{d\tau^2}+\boldsymbol{C}\omega_0\frac{d\Delta\boldsymbol{q}}{d\tau}+(\boldsymbol{K}+\boldsymbol{K}_{\text{nonlinear}})\Delta\boldsymbol{q}+\left(2\omega_0\boldsymbol{M}\frac{d^2\boldsymbol{q}_0}{d\tau^2}+C\frac{dq_0}{d\tau}\right)\Delta\omega}_{\text{Linear part}}$$
$$+\underbrace{\left((\boldsymbol{I}_n\otimes\Delta\boldsymbol{q}^{\mathrm{T}})\boldsymbol{h}_{\text{mc}}\Delta\boldsymbol{q}+\Delta\omega^2\boldsymbol{M}\frac{d^2\boldsymbol{q}_0}{d\tau^2}+2\Delta\omega\omega_0\boldsymbol{M}\frac{d^2\Delta\boldsymbol{q}}{d\tau^2}+\Delta\omega\boldsymbol{C}\frac{d\Delta\boldsymbol{q}}{d\tau}\right)}_{\text{Quadratic nonlinear part}}+\boldsymbol{r}=\boldsymbol{0}, \tag{4}$$

$$\boldsymbol{r}=\left(\omega_0^2\boldsymbol{M}\frac{d^2\boldsymbol{q}_0}{d\tau^2}+\boldsymbol{C}\omega_0\frac{d\boldsymbol{q}_0}{d\tau}+\boldsymbol{K}\boldsymbol{q}_0-\boldsymbol{G}(\boldsymbol{q}_0)\right)-\boldsymbol{F}\,cos(m\tau). \tag{5}$$

In the above equations, $\boldsymbol{r}$ is the unbalanced force of the system; $\boldsymbol{K}_{\text{nonlinear}}$ is the nonlinear stiffness matrix; and $\boldsymbol{h}_{\text{mc}}$ is the Hessian matrix formed by stacking the Hessian submatrices of each equation, which can be written as:

$$\boldsymbol{h}_{mc}=\frac{1}{2}\left[\frac{\partial^2G_1}{\partial\boldsymbol{q}\partial\boldsymbol{q}^T};\frac{\partial^2G_2}{\partial\boldsymbol{q}\partial\boldsymbol{q}^T};\cdots;\frac{\partial^2G_i}{\partial\boldsymbol{q}\partial\boldsymbol{q}^T};\cdots;\frac{\partial^2G_n}{\partial\boldsymbol{q}\partial\boldsymbol{q}^T}\right],\boldsymbol{K}_{\text{nonlinear}}=\frac{\partial\boldsymbol{G}}{\partial\boldsymbol{q}}. \tag{6}$$

Introducing an artificial asymptotic parameter ε allows Eq (4) to be expanded into a power series in ε, thereby decomposing the nonlinear problem into a sequence of linear subproblems that progressively approach the true solution and improve the convergence stability of the method. Equation (4) is thus rewritten as:

$$\underbrace{\omega_0^2\boldsymbol{M}\frac{d^2\Delta\boldsymbol{q}}{d\tau^2}+\boldsymbol{C}\omega_0\frac{d\Delta\boldsymbol{q}}{d\tau}+(\boldsymbol{K}+\boldsymbol{K}_{\text{nonlinear}})\Delta\boldsymbol{q}+\left(2\omega_0\boldsymbol{M}\frac{d^2\boldsymbol{q}_0}{d\tau^2}+\boldsymbol{C}\frac{d\boldsymbol{q}_0}{d\tau}\right)\Delta\omega}_{\text{Linear part}}$$
$$+\varepsilon\underbrace{\left((\mathbf{I}_n\otimes\Delta\boldsymbol{q}^{\mathrm{T}})\boldsymbol{h}_{\text{mc}}\Delta\boldsymbol{q}+\Delta\omega^2\boldsymbol{M}\frac{d^2\boldsymbol{q}_0}{d\tau^2}+2\Delta\omega\omega_0\boldsymbol{M}\frac{d^2\Delta\boldsymbol{q}}{d\tau^2}+\Delta\omega\boldsymbol{C}\frac{d\Delta\boldsymbol{q}}{d\tau}\right)}_{\text{Quadratic nonlinear part}}+\boldsymbol{r}=\boldsymbol{0}. \tag{7}$$

Expanding the incremental frequency $\Delta\omega$ and incremental displacement $\Delta\boldsymbol{q}$ into power series in the asymptotic parameter ε, $\Delta\boldsymbol{q}$ and $\Delta\omega$ can be written as:

$$\Delta\boldsymbol{q}(\tau,\varepsilon)=\sum_{k=0}^{M}\varepsilon^k\boldsymbol{y}_k,\qquad\Delta\omega(\varepsilon)=\sum_{k=0}^{M}\varepsilon^k\Delta\omega_k, \tag{8}$$

where M is the expansion order. Collecting coefficients of like powers of ε yields a sequence of equations:

$$\varepsilon^0:\ \omega_0^2\boldsymbol{M}\frac{d^2\boldsymbol{y}_0}{d\tau^2}+\boldsymbol{C}\omega_0\frac{d\boldsymbol{y}_0}{d\tau}+(\boldsymbol{K}+\boldsymbol{K}_{\text{nonlinear}})\boldsymbol{y}_0+\left(2\omega_0\boldsymbol{M}\frac{d^2\boldsymbol{q}_0}{d\tau^2}+\boldsymbol{C}\frac{d\boldsymbol{q}_0}{d\tau}\right)\Delta\omega_0=-\boldsymbol{r}, \tag{9}$$

$$\varepsilon^1:\ \omega_0^2\boldsymbol{M}\frac{d^2\boldsymbol{y}_1}{d\tau^2}+\boldsymbol{C}\omega_0\frac{d\boldsymbol{y}_1}{d\tau}+(\boldsymbol{K}+\boldsymbol{K}_{\text{nonlinear}})\boldsymbol{y}_1+\left(2\omega_0\boldsymbol{M}\frac{d^2\boldsymbol{q}_0}{d\tau^2}+\boldsymbol{C}\frac{d\boldsymbol{q}_0}{d\tau}\right)\Delta\omega_1$$

$$+\left((\mathbf{I}_n \otimes \boldsymbol{y}_0^{\mathrm{T}})\boldsymbol{h}_{\mathrm{mc}}\boldsymbol{y}_0 + \Delta\omega_0^2\boldsymbol{M}\frac{d^2\boldsymbol{q}_0}{d\tau^2} + 2\omega_0\Delta\omega_0\boldsymbol{M}\frac{d^2\boldsymbol{y}_0}{d\tau^2} + \Delta\omega_0\boldsymbol{C}\frac{d\boldsymbol{y}_0}{d\tau}\right) = 0, \tag{10}$$

$$\varepsilon^k\colon \omega_0^2\boldsymbol{M}\frac{d^2\boldsymbol{y}_k}{d\tau^2} + \boldsymbol{C}\omega_0\frac{d\boldsymbol{y}_k}{d\tau} + (\boldsymbol{K} + \boldsymbol{K}_{\mathrm{nonlinear}})\boldsymbol{y}_k + \left(2\omega_0\boldsymbol{M}\frac{d^2\boldsymbol{q}_0}{d\tau^2} + \boldsymbol{C}\frac{d\boldsymbol{q}_0}{d\tau}\right)\Delta\omega_k$$

$$+\sum_{i=0}^{k-1}\left(\left(\mathbf{I}_n \otimes \boldsymbol{y}_i^{\mathrm{T}}\right)\boldsymbol{h}_{\mathrm{mc}}\boldsymbol{y}_{k-1-i} + \Delta\omega_i\Delta\omega_{k-1-i}\boldsymbol{M}\frac{d^2\boldsymbol{q}_0}{d\tau^2}\right. \tag{11}$$

$$\left. + 2\omega_0\Delta\omega_i\boldsymbol{M}\frac{d^2\boldsymbol{y}_{k-1-i}}{d\tau^2}\Delta\omega_i\boldsymbol{C}\frac{d\boldsymbol{y}_{k-1-i}}{d\tau}\right) = 0.$$

By solving the above sequence of linear matrix equations, the total increment is obtained by superposition of the incremental solutions at each order, i.e.,

$$\Delta\boldsymbol{q}(\tau,\varepsilon) = \sum_{k=0}^{M}\boldsymbol{y}_k\,, \qquad \Delta\omega(\varepsilon) = \sum_{k=0}^{M}\Delta\omega_k. \tag{12}$$

2.2. Harmonic balance procedure

The second stage of TRE-IHB is the harmonic balance procedure. After completing the asymptotic expansion, harmonic balance is applied to each linear sequence subproblem to transform the time-domain equations into frequency-domain algebraic equations. In the incremental harmonic balance method, harmonic balance is implemented through the basis-function matrix $\boldsymbol{S}$. Let the harmonic truncation number be N_s; the basis-function matrix is:

$$\boldsymbol{S} = diag(\boldsymbol{C}_S, \boldsymbol{C}_S, \ldots\ldots \boldsymbol{C}_S), \tag{13}$$

where

$$\boldsymbol{C}_S = [1, \cos\tau\,, \sin\tau\,, \cos 2\tau\,, \sin 2\tau\,, \cos 3\tau\,, \sin 3\tau\,, \ldots\ldots, \cos(N_s\tau), \sin(N_s\tau)].$$

Since the periodic solution is composed of different harmonic components, the periodic initial solution and the increment $\boldsymbol{y}_k$ of the k-th linear matrix equation can be written as

$$\boldsymbol{q}_0 = S\boldsymbol{A}_0, \boldsymbol{y}_k = \boldsymbol{S}\Delta\boldsymbol{A}_k, \tag{14}$$

where

$$\boldsymbol{A}_0 = \left[a_{10}, a_{11}, b_{11}, \ldots\ldots, a_{1N_s}, b_{1N_s}, a_{20}, \ldots\ldots, b_{nN_s}\right]^T,$$

$$\boldsymbol{\Delta A}_k = \left[\Delta a_{10}^{(k)}, \Delta a_{11}^{(k)}, \Delta b_{11}^{(k)} \ldots\ldots, \Delta a_{1N_s}^{(k)}, \Delta b_{1N_s}^{(k)}, \Delta a_{20}^{(k)}, \ldots\ldots, \Delta b_{nN_s}^{(k)}\right]^T.$$

Substituting Eqs (13) and (14) into the sequence of linear equations and applying the Galerkin method yields the frequency-domain equation of the k-th linear matrix equation:

$$\boldsymbol{K}_{\mathrm{mc}}\Delta\boldsymbol{A}_k + \boldsymbol{R}_{\mathrm{mc}}\Delta\omega_k + \boldsymbol{R}_k = \boldsymbol{0}, \tag{15}$$

where

$$\boldsymbol{R}_0 = \int_0^{2\pi} \boldsymbol{S}^{\mathrm{T}} \cdot \left(\omega_0^2 \boldsymbol{M}\frac{d^2 q_0}{d\tau^2} - \boldsymbol{C}\omega_0\frac{d\boldsymbol{q}_0}{d\tau} - \boldsymbol{K}\boldsymbol{q}_0 - \boldsymbol{G}(\boldsymbol{q}_0) - \boldsymbol{F}\,cos(m\tau)\right)d\tau,$$

$$\boldsymbol{K}_{\mathrm{mc}} = \int_0^{2\pi} \boldsymbol{S}^{\mathrm{T}} \cdot \left(\omega_0^2 \boldsymbol{M}\frac{d^2\boldsymbol{S}}{d\tau^2} + \boldsymbol{C}\omega_0\frac{d\boldsymbol{S}}{d\tau} + (\boldsymbol{K} + \boldsymbol{K}_{\mathrm{nonlinear}})\boldsymbol{S}\right)d\tau,$$

$$\boldsymbol{R}_{\mathrm{mc}} = \int_0^{2\pi} \boldsymbol{S}^{\mathrm{T}} \cdot \left(2\omega_0 \boldsymbol{M}\frac{d^2\boldsymbol{q}_0}{d\tau^2} + \boldsymbol{C}\frac{d\boldsymbol{q}_0}{d\tau}\right)d\tau, \boldsymbol{M}_{\mathrm{mc}} = \int_0^{2\pi} \boldsymbol{S}^{\mathrm{T}}\,\boldsymbol{M}\frac{d^2\boldsymbol{q}_0}{d\tau^2}\,d\tau,$$

$$\boldsymbol{H}_{\mathrm{mc}}^{(i)} = \int_0^{2\pi} \boldsymbol{C}_S^{\mathrm{T}} \otimes \boldsymbol{h}_{\mathrm{mc}}^{(i)}\boldsymbol{S}d\tau, \boldsymbol{H}_{\mathrm{mc}} = \left[\boldsymbol{H}_{\mathrm{mc}}^{(1)}; \boldsymbol{H}_{\mathrm{mc}}^{(2)}; \boldsymbol{H}_{\mathrm{mc}}^{(3)}; \cdots; \boldsymbol{H}_{\mathrm{mc}}^{(i)}; \cdots; \boldsymbol{H}_{\mathrm{mc}}^{(n)}\right],$$

$$R_k = \sum_{i=0}^{k-1}\left(\mathbf{I}_{2N_s+1} \otimes \Delta\boldsymbol{A}_i^{\mathrm{T}}\right)\boldsymbol{H}_{\mathrm{mc}}\Delta\boldsymbol{A}_{k-1-i} + \sum_{i=0}^{k-1}\Delta\omega_i\boldsymbol{M}_{\mathrm{mc}}\Delta\omega_{k-1-i} + \sum_{i=0}^{k-1}\Delta\omega_i\boldsymbol{R}_{\mathrm{mc}}\Delta\boldsymbol{A}_{k-1-i}.$$

In the above equations, $\boldsymbol{R}_0$ is the error matrix, $\boldsymbol{K}_{\mathrm{mc}}$ is the tangent matrix, $\boldsymbol{R}_{\mathrm{mc}}$ is the frequency matrix, $\boldsymbol{M}_{\mathrm{mc}}$ is the mass–displacement matrix, $\boldsymbol{H}_{\mathrm{mc}}$ is the Hessian matrix, and $\boldsymbol{R}_k$ is the sequence error matrix. In a single iteration step, during the recursion, the above matrices are constant matrices. In each sequence of linear equations, the number of unknowns is one more than the number of equations; therefore, the sequence of matrix equations constitutes an underdetermined system. When solving a nonlinear system with a known external excitation frequency, the parameter ω remains unchanged, $\boldsymbol{R}_{\mathrm{mc}} = 0$, and the k-th sequence matrix equation can be simplified as:

$$\boldsymbol{K}_{\mathrm{mc}}\Delta\boldsymbol{A}_k + \boldsymbol{R}_k = \boldsymbol{0}, \tag{16}$$

where $\Delta\boldsymbol{A}_k$ can be obtained from $\Delta\boldsymbol{A}_k = -\boldsymbol{K}_{\mathrm{mc}}^{-1}\boldsymbol{R}_k$, and then $\boldsymbol{A} = \boldsymbol{A} + \sum_{i=0}^{k}\Delta\boldsymbol{A}_k = \boldsymbol{A} + \Delta\boldsymbol{A}$ is used to update $\boldsymbol{A}$ until the convergence criterion $\| \boldsymbol{R}_0 \| \leq 10^{-10}$ is satisfied.

2.3. Coupling with the trust-region dogleg method

The solution of the k-th sequence subproblem (16) is formulated as a nonlinear least-squares problem:

$$\arg\min f(A) = \frac{1}{2}\| \boldsymbol{R} + \boldsymbol{R}_k - \boldsymbol{R}_0 \|^2. \tag{17}$$

When $k = 0$, $\boldsymbol{R}_k = \boldsymbol{R}_0$. At the iterate $\boldsymbol{A}_0$, the Gauss–Newton local model is constructed as

$$m\left(\Delta\boldsymbol{A}_{k\_\mathrm{candidate}}\right) = \frac{1}{2}\| \boldsymbol{R}_k + \boldsymbol{K}_{\mathrm{mc}}\Delta\boldsymbol{A}_{k_{\mathrm{candidate}}} \|^2. \tag{18}$$

In the solution process of the Gauss–Newton local model, $\triangle \boldsymbol{A}_{k\_\mathrm{candidate}}$ is constrained within the trust region, whose radius is Δ_k. The trust-region dogleg method constructs the search path by combining the steepest-descent direction (Cauchy point) and the Gauss–Newton direction. The trust-region gradient direction $\boldsymbol{g}_k$, the Cauchy point $\boldsymbol{S}_{\mathrm{C}}^k$, and the Gauss–Newton point S_{GN}^k are given by

$$\boldsymbol{g}_k \triangleq \nabla f(\boldsymbol{A}) = \nabla\left(\frac{1}{2}\|\boldsymbol{R} + \boldsymbol{R}_k - \boldsymbol{R}_0\|^2\right) = \boldsymbol{K}_{\mathrm{mc}}^{\mathrm{T}}\boldsymbol{R}_k, \tag{19}$$

$$\boldsymbol{S}_{\mathrm{C}}^k = -\|\boldsymbol{g}_k\|^2/((\boldsymbol{K}_{\mathrm{mc}}^T\boldsymbol{g}_k)^{\mathrm{T}}\boldsymbol{K}_{\mathrm{mc}}\boldsymbol{g}_k)\,\boldsymbol{g}_k, \tag{20}$$

$$\boldsymbol{S}_{\mathrm{GN}}^k = -(\boldsymbol{K}_{\mathrm{mc}}^T\boldsymbol{g}_k)^{-1}\boldsymbol{K}_{\mathrm{mc}}^T\boldsymbol{R}_k. \tag{21}$$

According to the trust-region algorithm [37], when $\|\boldsymbol{S}_{\mathrm{GN}}^k\| \le \Delta_k$, $\Delta\boldsymbol{A}_{k\_\mathrm{candidate}} = \boldsymbol{S}_{\mathrm{GN}}^k$; when $\|\boldsymbol{S}_{\mathrm{C}}^k\| \ge \Delta_k$, $\Delta\boldsymbol{A}_{k\_\mathrm{candidate}} = (\Delta_k/\|S_{\mathrm{C}}^k\|)\boldsymbol{S}_{\mathrm{C}}^k$; when $\|\boldsymbol{S}_{\mathrm{C}}^k\| < \Delta_k < \|\boldsymbol{S}_{\mathrm{GN}}^k\|$, $\Delta\boldsymbol{A}_{k\_\mathrm{candidate}}$ is selected on the dogleg path (the line segment connecting $\boldsymbol{S}_C^k$ and $\boldsymbol{S}_{GN}^k$) at the point satisfying $\|\Delta\boldsymbol{A}_{k\_\mathrm{candidate}}\| = \Delta_k$.

Using Eqs (17) and (18), two measures are introduced, and the ratio of the actual reduction to the predicted reduction is computed as follows:

$$\rho_k = \left(f(\boldsymbol{A}) - f\left(\boldsymbol{A} + \Delta\boldsymbol{A}_{k\_\mathrm{candidate}}\right)\right)/\left(m(0) - m\left(\Delta\boldsymbol{A}_{k\_\mathrm{candidate}}\right)\right). \tag{22}$$

To ensure the effectiveness of the asymptotic expansion procedure, after each subproblem at a given order is solved, the error matrix R should decrease, i.e.,

$$\mathrm{tol}_k = \left\|\boldsymbol{R}\left(\boldsymbol{A} + \sum_{i=0}^{k-1}\boldsymbol{\Delta A}_{k-1}\right)\right\| - \left\|\boldsymbol{R}\left(\boldsymbol{A} + \sum_{\boldsymbol{i=0}}^{k-1}\boldsymbol{\Delta A}_{k-1} + \boldsymbol{\Delta A}_{k_{\mathrm{candidate}}}\right)\right\|. \tag{23}$$

It should be noted that, according to the principle of asymptotic expansion, when $\|\Delta\boldsymbol{A}_{k\_\mathrm{candidate}}\|/\|\Delta\boldsymbol{A}_{k-1}\| > 1$, TRE-IHB may become unstable and diverge. Therefore, in the k-th trust-region algorithm, the trust-region radius should be the minimum of the trust-region radius Δ_k in the k-th linear matrix equation and $\|\Delta\boldsymbol{A}_{k-1}\|$. In addition, when $\|\Delta\boldsymbol{A}_k\| < 0.01\|\Delta\boldsymbol{A}_0\|$, the increment $\Delta\boldsymbol{A}_k$ can be regarded as negligible; at this point, the asymptotic expansion sequence is truncated, the expansion order M in Eq (8) is determined, and the procedure proceeds to the next loop. The specific algorithm is given in Algorithm 1.

Algorithm 1. Trust-region dogleg algorithm for the k-th sequence subproblem.

Date: $\rho_k, \Delta_k, \mathrm{tol}_k, \Delta \boldsymbol{A}_{k\_\mathrm{candidate}}$

Result: Δ_{k+1}, $\Delta \boldsymbol{A}_k$

if $\rho_k > 0.75$ &&$\mathrm{tol}_k > 0$

  $\Delta \boldsymbol{A}_k = \Delta \boldsymbol{A}_{k\_\mathrm{candidate}}, \Delta_{k+1} = \min(2\Delta_k, \| \Delta \boldsymbol{A}_k \|)$; break;

else if $0.5 \le \rho_k \le 0.75$&&$\mathrm{tol}_k > 0$

  $\Delta \boldsymbol{A}_k = \Delta \boldsymbol{A}_{k\_\mathrm{candidate}}$, $\Delta_{k+1} = \min(\Delta_k, \| \Delta \boldsymbol{A}_k \|)$; break;

else if $0.1 < \rho_k < 0.5$&&$\mathrm{tol}_k > 0$

  $\Delta \boldsymbol{A}_k = \Delta \boldsymbol{A}_{k\_\mathrm{candidate}}, \Delta_{k+1} = \min(0.5\Delta_k, \| \Delta \boldsymbol{A}_k \|)$; break;

else

  $\Delta_k = \max(0.5\Delta_k, \Delta_{\min})$; continue;

end

if $\|\Delta \boldsymbol{A}_k\| < 0.01\|\Delta \boldsymbol{A}_0\|$

  $\Delta \boldsymbol{A}_k = \boldsymbol{0}$; break;

end

To further enhance the capability of escaping local plateaus, a stagnation detection mechanism and a jump–backtracking step strategy are introduced. The stagnation indicator γ_f is defined as the relative decrease of the objective function over consecutive iterations:

$$\gamma_f = \left(\| \boldsymbol{R}_0^{(n+1)} \| - \| \boldsymbol{R}_0^{(n)} \| \right) / \| \boldsymbol{R}_0^n \|. \tag{24}$$

When $\gamma_f > 10^{-4}$, the iterate $\boldsymbol{A}$ and the trust-region radius $\Delta_0^{(n+1)}$ are updated. When $\gamma_f \le 10^{-4}$, the system is considered to be stalled. Depending on the parity of the adjustment count, a jump step (expanding the step size along the gradient direction while shrinking the trust-region radius) or a backtracking step (returning to the most recent better iterate while shrinking the trust-region radius) is alternately executed. The specific algorithm is given in algorithm 2.

The above trust-region solver is embedded into the solution loop of each asymptotic subproblem at every order, which ensures the numerical stability and convergence of the solution for each subproblem.

Algorithm 2. Jump–backtracking strategy in the trust-region algorithm

Date:$\gamma_f, \boldsymbol{g}_k, \boldsymbol{A}_0, n_1, \Delta_0^{(n)}, \rho_0^{(n)}, \boldsymbol{A}_n$

Result: $\boldsymbol{A}_{n+1},\ \Delta_0^{(n+1)},\ \Delta_{\max}$

if $\| \gamma_f \| > 10^{-4}$

  $\boldsymbol{A}_{n+1} = \boldsymbol{A}_n + \sum_{k=0} \Delta \boldsymbol{A}_k$

  If $\rho_0^{(n)} > 0.75$

    $\Delta_0^{(n+1)} = \min\left(2\Delta_0^{(n)}, \Delta_{\max}\right)$

  else if $0.5 \le \rho_0^{(n)} \le 0.75$

    $\Delta_0^{(n+1)} = \Delta_0^{(n)}$

  else if $0.1 < \rho_0^{(n)} < 0.5$

    $\Delta_0^{(n+1)} = 0.5\Delta_0^{(n)}$

  end

else if $\mathrm{mod}(n_1, 2) = 0$

  $\boldsymbol{A}_{n+1} = \boldsymbol{A}_n - \frac{\boldsymbol{g}_k}{\|\boldsymbol{g}_k\|}(n_1+1); \Delta_0^{(n+1)} = \frac{\|\boldsymbol{A}_{n+1}\|}{(n_1+1)};\ \Delta_{\max} = 10\Delta_0^{(n_1+1)}; n_1 = n_1 + 1;$

else if $\mathrm{mod}(n_1, 2) = 1$

  $\boldsymbol{A}_{n+1} = \boldsymbol{A}_0;\ \Delta_0^{(n+1)} = \frac{\|\boldsymbol{A}_0\|}{(n_1+1)};\ \Delta_{\max} = 10\Delta_0^{(n_1+1)}; n_1 = n_1 + 1;$

end

The three mechanisms above make TRE-IHB less sensitive to initial guesses. First, asymptotic expansion decomposes the nonlinear problem into a series of linear subproblems, correcting errors step by step and avoiding large jumps. Second, the trust-region solver adaptively limits the step size, ensuring convergence even when the initial guess is poor. Third, the jump–backtracking mechanism helps the algorithm escape stagnation caused by bad initial guesses. Together, these features significantly widen the convergence basin and stabilize the iteration process compared with traditional IHB.

3. Stability analysis of periodic solutions and arc-length continuation

After obtaining the periodic response of the system, its stability needs to be further analyzed, and the branches of the solution curve under parameter variations should be tracked. This section first establishes a stability criterion for periodic solutions based on Floquet theory, and then introduces an

adaptive arc-length continuation algorithm within a predictor-corrector framework for complete tracking of the response curve.

3.1. Stability of periodic responses

After a periodic solution is obtained, its stability can be analyzed by applying a small perturbation $\boldsymbol{\Delta q}$. The perturbation equation can be written as:

$$\omega_0^2 \boldsymbol{M} \frac{d^2 \boldsymbol{\Delta q}}{d\tau^2} + \omega_0 \boldsymbol{C} \frac{d\boldsymbol{\Delta q}}{d\tau} + (\boldsymbol{K} + \boldsymbol{K}_{\text{nonlinear}}) \boldsymbol{\Delta q} = 0. \tag{25}$$

Equation (25) is rewritten in the first-order state-space form:

$$\frac{d\boldsymbol{X}}{d\tau} = \boldsymbol{Q}(\tau)\boldsymbol{X}, \tag{26}$$

where

$$\boldsymbol{X} = \left[\Delta \boldsymbol{q} \quad \frac{d\Delta q}{d\tau}\right]^{\mathrm{T}}, \boldsymbol{Q} = \begin{bmatrix} 0 & \boldsymbol{I} \\ -\dfrac{\boldsymbol{M}^{-1}(\boldsymbol{K} + 3\boldsymbol{K}_{\text{nonlinear}})}{\omega^2} & -\dfrac{\boldsymbol{M}^{-1}C}{\omega} \end{bmatrix}.$$

$\boldsymbol{Q}$ is a periodic matrix with period T. For Eq (25), there exists a fundamental solution:

$$z_k = [z_{1k} \quad z_{2k} \quad \cdots\cdots \quad z_{Nk}]^{\mathrm{T}}, k = 1,2,\ldots\ldots,N, \tag{27}$$

where $N = 2n$. The fundamental solutions can be written in matrix form as:

$$Z = \begin{bmatrix} z_{11} & z_{12} & \cdots & z_{1N} \\ z_{21} & z_{22} & \cdots & z_{2N} \\ \vdots & \vdots & & \vdots \\ z_{N1} & z_{N2} & \cdots & z_{NN} \end{bmatrix}. \tag{28}$$

Clearly, $\boldsymbol{Z}$ satisfies the matrix equation

$$\frac{d\boldsymbol{Z}}{d\tau} = \boldsymbol{Q}(\tau)\boldsymbol{Z}. \tag{29}$$

Since $\boldsymbol{Q}(\tau) = \boldsymbol{Q}(\tau + T)$, $\boldsymbol{Z}(\tau + T)$ is also a fundamental matrix solution and can thus be expressed as:

$$\boldsymbol{Z}(\tau + T) = \boldsymbol{P}\boldsymbol{Z}(\tau), \tag{30}$$

where $\boldsymbol{P}$ is a nonsingular constant matrix. According to Floquet theory [16], the stability criterion depends on the eigenvalues of $\boldsymbol{P}$. If the absolute values of all eigenvalues of $\boldsymbol{P}$ are less than 1, the solution is asymptotically stable; otherwise, the motion is unstable. For further discussion, the period T is divided into N_k parts. In the k-th time interval with $\Delta_k = \tau_k - \tau_{k-1}$, the periodic coefficient matrix $\boldsymbol{Q}(\tau)$ is replaced by a constant matrix $\boldsymbol{Q}_k$:

$$\boldsymbol{Q}_k = \frac{1}{\Delta_k} \int_{\tau_{k-1}}^{\tau_k} Q(\xi)\, d\xi. \tag{31}$$

Finally, the transfer matrix $\boldsymbol{P}$ is expressed as

$$\boldsymbol{P} = Z(T) = \prod_{i=1}^{N_k} \left[I + \sum_{j=1}^{N_j} \frac{(\Delta_i Q_i)^j}{j!} \right]. \tag{32}$$

In this paper, the above stability analysis is automatically executed after each periodic solution is obtained. In the figures, solid lines (stable) and dashed lines (unstable) are used for distinction.

3.2. Arc-length continuation

To overcome tracking failure of the frequency response curve at turning points or branch points due to Jacobian singularity, an adaptive arc-length continuation method is adopted to obtain the system response curve. This method treats the curve arc length itself as the continuation parameter and achieves robust advancement of the solution through a predictor–corrector framework.

Define the solution vector $\boldsymbol{x} = [\omega, \boldsymbol{A}]^{\mathrm{T}}$. The distance between two adjacent solution points is the local arc length $S_i = \|\boldsymbol{x}_i - \boldsymbol{x}_{i-1}\|$, and the accumulated arc length is $\boldsymbol{t}_i = \sum_{k=1}^{i} S_k$. If the arc-length increment at the current point is ΔS_i, then the accumulated arc length of the next target point is $t_{i+1} = t_i + \Delta S_i$. Using the latest four consecutive solution points x_{i-3}, x_{i-2}, x_{i-1}, x_i and their corresponding accumulated arc lengths, the initial predictor for the next iteration can be extrapolated by cubic Lagrange interpolation [38]:

$$\boldsymbol{x}_{i+1} = \sum_{r=l-3}^{i} \left(\prod_{\substack{p=i-3 \\ r \neq p}}^{i} \frac{t_{i+1} - t_p}{t_r - t_p} \right) \boldsymbol{x}_r. \tag{33}$$

Adaptive control of the arc-length step size is crucial to the efficiency and stability of the algorithm. In this paper, the step size is dynamically adjusted according to the convergence behavior of the previous corrected point:

$$\Delta S_i = 3\,\Delta S_{i-1}/n. \tag{34}$$

Where n is the number of iterations required for the TRE-IIHB method to reach convergence at solution point x_i. This strategy allows a larger step size in regions where the response curve is smooth to improve efficiency, while automatically shrinking the step size in regions with large curvature or strong nonlinearity to ensure numerical stability. To avoid singularity during the correction process, the dominant iterative variable should be selected according to the offset direction of the predicted point:

$$k_x = \max_j \left(x_{i+1,j} - x_{i,j} \right). \tag{35}$$

If $k_x = 1$, the change in the frequency direction dominates; thus, ω is fixed in this step, and only $\Delta \boldsymbol{A}$ is iterated. If $k_x > 1$, the corresponding component in $\boldsymbol{A}$ is fixed, and ω is taken as the iterative variable. Accordingly, the system Jacobian matrix $\boldsymbol{K}_{\mathrm{mc}}$, the displacement increment matrix $\Delta \boldsymbol{A}_k$, and the frequency increment $\Delta \omega_k$ are adjusted as:

$$\begin{aligned} \boldsymbol{K}_{\mathrm{mc}} &= [\boldsymbol{K}_{\mathrm{mc}}(:,1{:}\,k_x-1) \quad \boldsymbol{R}_{\mathrm{mc}} \quad \boldsymbol{K}_{\mathrm{mc}}(:,k_x+1{:}\,end)], \\ \Delta\boldsymbol{A}_k &= [\Delta\boldsymbol{A}_k(:,1{:}\,k_x-1) \quad 0 \quad \Delta\boldsymbol{A}_k(:,k_x+1{:}\,end)], \\ \Delta\omega_k &= \Delta\boldsymbol{A}_k(:,k_x). \end{aligned} \tag{36}$$

The proposed method couples the above arc-length continuation mechanism with the TRE-IIHB solver. The complete computational procedure is shown in Figure 1. The flow mainly consists of two stages: Stage 1 computes the first four points on the response curve, providing the data basis for cubic interpolation prediction, and Stage 2 performs prediction–correction in a loop under adaptive arc-length control, thereby achieving complete and robust tracking of the system frequency response curve. The proposed method couples the above arc-length continuation mechanism with the TRE-IHB solver. In this framework, the effectiveness of the predictor relies on cubic Lagrange interpolation. Compared with linear or quadratic schemes, cubic interpolation captures the local curvature of the solution branch more accurately. With a properly chosen arc-length step ΔS_i, the local truncation error is $O\left(\Delta S^4\right)$, ensuring that the predicted point x_{i+1} lies sufficiently close to the true solution, thereby providing a high-quality initial guess for the corrector stage. The corrector stage solves for the exact solution using the TRE-IHB iteration, with the predicted point x_{i+1} as the initial guess. Convergence is declared when the residual norm satisfies $\|\boldsymbol{R}_0\| \le 10^{-10}$. If the corrector fails to converge within a prescribed maximum number of iterations (e.g., 20) or the residual increases, the step size ΔS_i is halved, and a new prediction–correction cycle is initiated. This adaptive strategy, together with Eq (34), ensures robust tracking of the frequency response curve even near turning points or bifurcations.

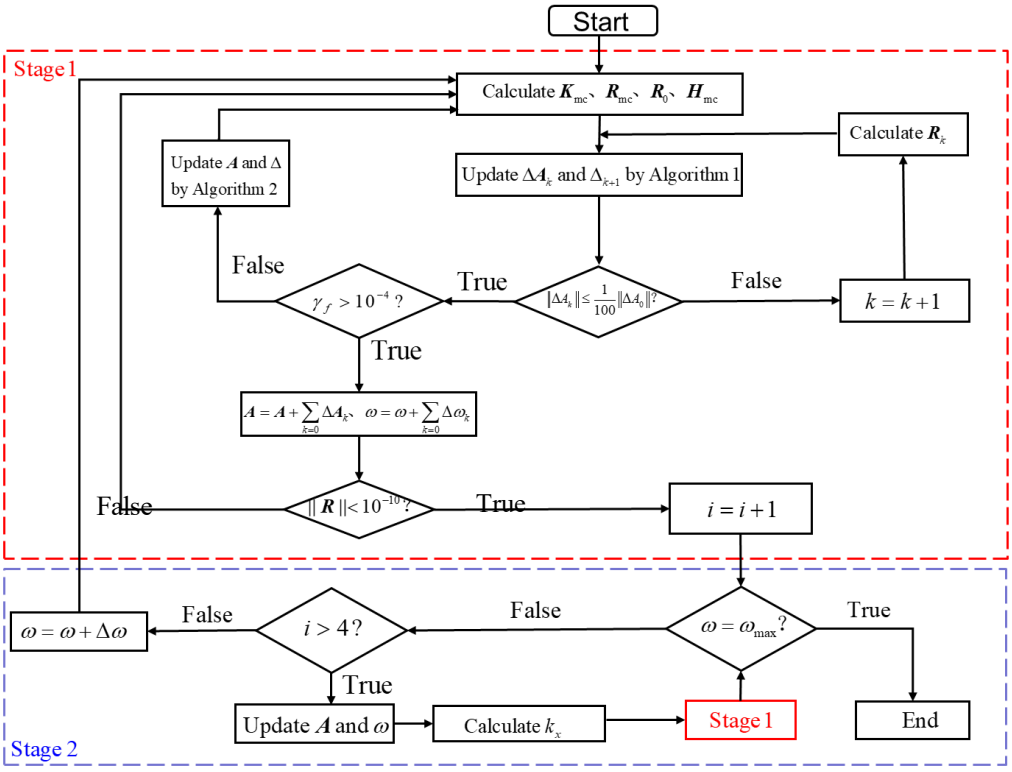

Figure 1. Flowchart of the TRE-IHB algorithm.

4. Numerical examples

The proposed TRE-IHB method is systematically validated through three representative strongly nonlinear equations: the Van der Pol–Mathieu equation, the axially moving belt/plate equation, and the Bouc–Wen hysteretic equation. The results are compared with those obtained by the Runge–Kutta method (RK), the IHB method, and the TRE-IHB method. The comparisons are conducted from four aspects (the basin of convergence, number of iterations, convergence process, and computing time), in order to comprehensively evaluate the robustness and efficiency of the method.

4.1. Periodic response of the Van der Pol–Mathieu equation

The Van der Pol–Mathieu equation is commonly used to describe an oscillatory system with nonlinear damping under parametric excitation, and its typical characteristics include parametric resonance and limit-cycle oscillations [39]. The dynamical model of the system is shown in Figure 2.

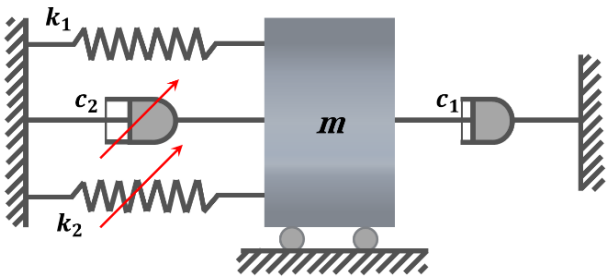

Figure 2. Dynamical model of the Van der Pol–Mathieu equation.

Its nonlinear equation is

$$m\frac{d^2q}{dt^2} - (c_1 - c_2q^2)\frac{dq}{dt} + (k_1 + k_2\cos(2\Omega t))q = 0, \tag{37}$$

where c_1 is the linear damping coefficient, c_2 is the nonlinear damping coefficient, k_1 is the linear stiffness coefficient, and k_2 and ω_0 are the amplitude and frequency of the parametric excitation, respectively. For convenience in interpretation and computation, Eq (37) is nondimensionalized by defining:

$$\omega_0^2 = k_1/m\,, \omega = \Omega/\omega_0\,; \alpha_1 = c_1\sqrt{1/mk_1}\,, \alpha_2 = c_2\sqrt{1/mk_1}\,, \beta = k_2/k_1\,, \Omega t = \omega\tau_1.$$

Then, Eq (36) becomes

$$\frac{d^2q}{d\tau_1^2} - (\alpha_1 - \alpha_2q^2)\frac{dq}{d\tau_1} + (1 + \beta\cos(2\omega\tau_1))q = 0. \tag{38}$$

Let $\tau = \omega\tau_1$. The periodic solution of Eq (38) can be expressed as:

$$q(\tau) = \sum_{i=1}^{3} a_{2i-1}\cos(2i-1)\tau + b_{2i-1}\sin(2i-1)\tau. \tag{39}$$

First, the periodic response of the system is computed for $\alpha_1 = 0.01$, $\alpha_2 = 0.01$, $\alpha_3 = 0.05$, and $\omega = 1$. These parameter values are adopted from [39]. Figure 3 compares the time histories and phase portraits obtained by the fourth-order RK method, the IHB method, and the proposed TRE-IHB method. The results of the three methods agree closely, which verifies that TRE-IHB achieves computational accuracy comparable to that of the conventional methods for strongly nonlinear systems and does not introduce additional errors due to the incorporation of the asymptotic expansion and trust-region strategy.

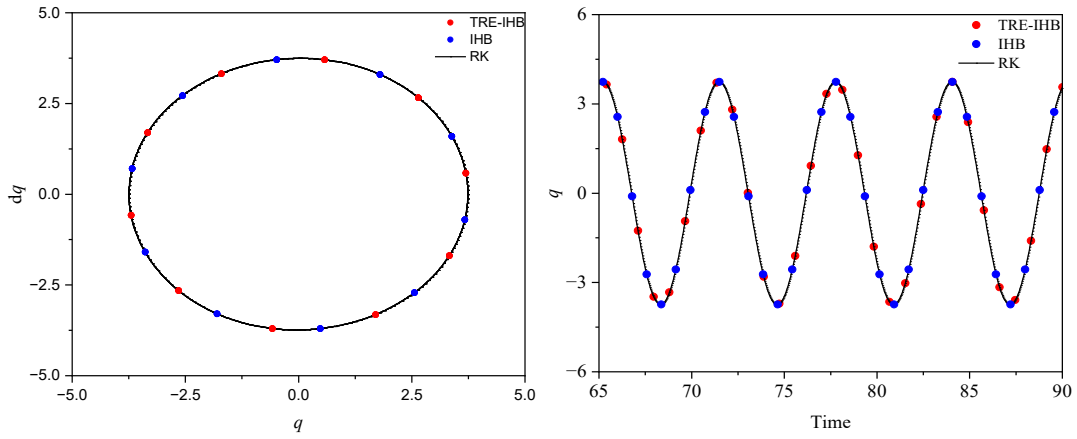

Figure 3. Periodic response of the Van der Pol–Mathieu equation for $\omega = 1$: (a) time history; (b) phase portrait.

To examine the robustness of the algorithms with respect to the initial guess, 3600 points were uniformly sampled over the parameter plane spanned by the initial harmonic coefficients a_1 and a_3 (with the remaining harmonic coefficients set to 0) within the domain $[-10, 10] \times [-10, 10]$ for convergence tests. Figure 4 shows the distributions of the basins of convergence for the IHB and TRE-IHB methods. When a_1 is close to zero, IHB is difficult to converge; its initial guess is prone to fall into a physically meaningless zero solution, as shown in Figure 4(a). In contrast, the convergence points of TRE-IHB cover the entire parameter plane, as shown in Figure 4(b). This indicates that TRE-IHB markedly reduces dependence on the initial guess and effectively broadens the basin of convergence. This improvement is mainly attributable to the serialized decoupling of the nonlinear problem in the asymptotic expansion procedure and the adaptive constraint on the iteration step size provided by the trust-region mechanism; together, they prevent incorrect iteration trajectories.

To further clarify the differences in iterative behavior between the two methods, Figure 5 presents the iteration process starting from the same initial point $(a_1 = -0.5,\ a_3 = -4.5)$. Although both methods reduce the residual to a low level within five iterations, their convergence trajectories reveal a fundamental difference. In IHB, the residual continues to decrease, but the amplitude of the solution vector keeps decaying, and the iteration ultimately converges to the zero solution. In contrast, in TRE-

IHB, owing to the serialized treatment in the asymptotic expansion and the step-size control of the trust region in the first iteration, the update step is more cautious; the residual decreases more gradually, while the solution vector retains its nonzero physical meaning, and the iteration then steadily approaches the true periodic solution. This confirms that the proposed method can effectively avoid the "zero-solution trap" and ensure convergence to a physically meaningful response.

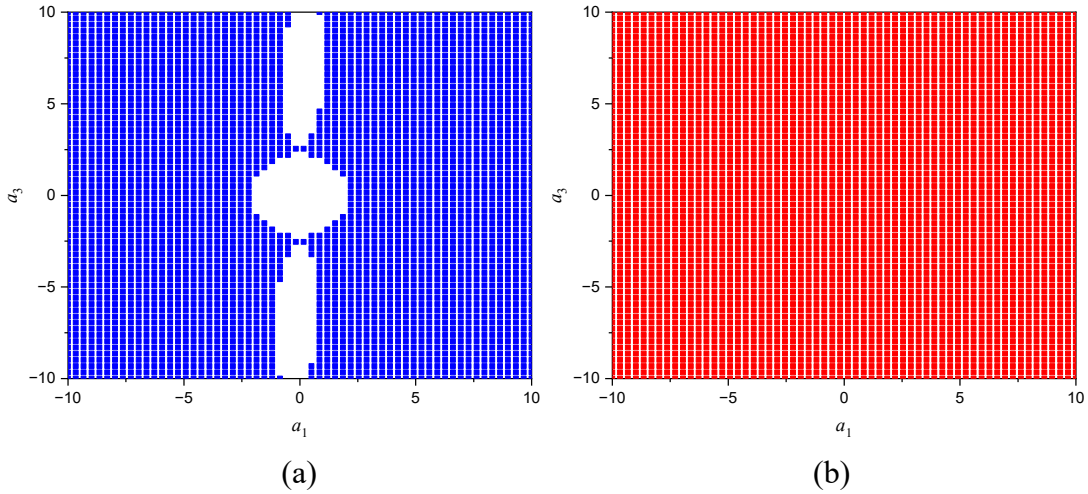

Figure 4. Basins of convergence for different initial values a_1, a_3: (a) IHB; (b) TRE-IHB.

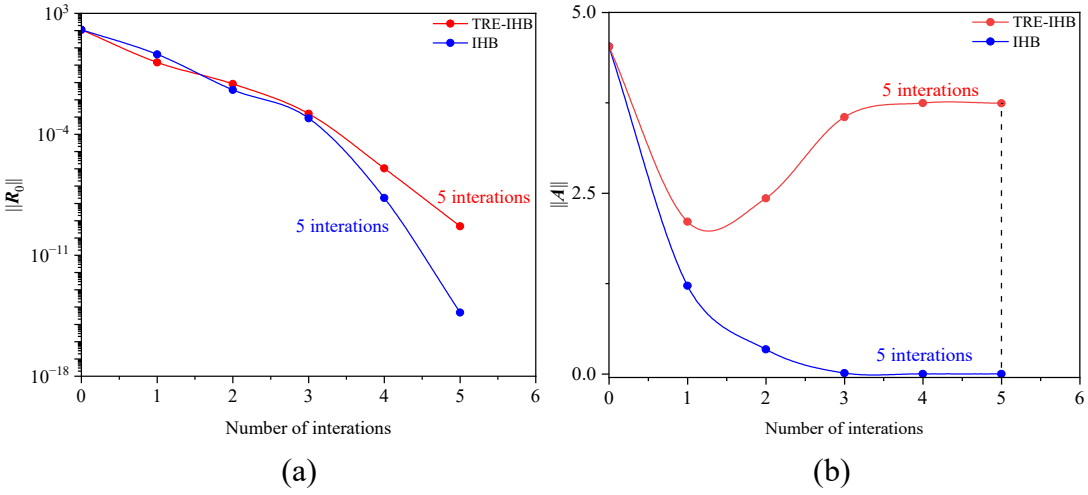

Figure 5. Iteration process for $a_1 = -0.5$, $a_3 = -4.5$ with the other harmonic coefficients set to 0: (a) variation of $\| R_0 \|$ during the iterations; (b) variation of $\| A \|$ during the iterations.

The overall performance of the proposed method is further reflected in the parametric sweep. Figure 6 shows the frequency-amplitude response curves of the system for different linear damping coefficients β, where dashed and solid lines denote unstable and stable solutions, respectively. Unlike the Runge–Kutta method, which can capture only stable periodic solutions, both IHB and TRE-IHB can simultaneously obtain the stable and unstable branches of the system. As β decreases from 0.05 to 0.01, the response curves gradually contract near $\omega \approx 1$ and form a closed hysteresis loop.

Such strongly nonlinear characteristics impose higher demands on algorithmic stability and step-size control.

It is worth clarifying that the number of points on the frequency-response curve is primarily determined by the arc-length step size. Conventional IHB, due to its poor corrector robustness, is forced to drastically reduce the step size in strongly nonlinear regions (such as near the hysteresis loop in Figure 6) to maintain convergence, resulting in a large number of points. In contrast, TRE-IHB introduces a trust-region mechanism and asymptotic expansion, making the corrector much more robust. This robustness allows the arc-length controller to proactively take larger steps [Eq (34)] and trace the curve with far fewer points. As shown in Table 1, for $\beta = 0.01$, TRE-IHB requires only 30 points (compared with 88 for IHB), and the computing time is reduced from 147.22 to 54.57 s (approximately 37%). Therefore, the significant reduction in the number of points is not an arbitrary choice of arc-length parameters but a direct manifestation of the improved robustness of the TRE-IHB method itself. Together with the reduction in iterations per point, this leads to a clear gain in computational efficiency.

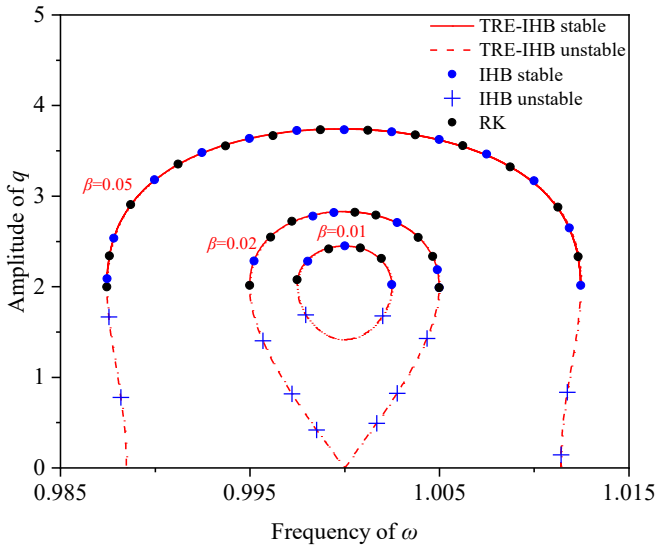

Figure 6. Frequency-amplitude response curves of the Van der Pol–Mathieu equation.

Table 1. Related results for the frequency–amplitude response curves in Figure 6.

Method	β	Number of points	Total iterations	Total computing time (s)
IHB	0.01	88	203	147.22
TRE-IHB	0.01	30	83	54.57
IHB	0.02	96	228	169.95
TRE-IHB	0.02	34	76	48.21
IHB	0.05	121	264	199.30
TRE-IHB	0.05	31	73	46.34

4.2. Periodic response of the axially moving equation

Axially moving equations are widely encountered in engineering fields such as rolling processes and belt transportation, and their dynamic behavior often exhibits complex features arising from the coupling of internal resonance and geometric nonlinearity [40]. Taking an axially moving belt model as an example (Figure 7), the axially moving belt has density ρ, cross-sectional area A, flexural rigidity D, axial tension T, span length L between two supports, belt width b, damping coefficient c_0, transport speed V_0, external load F_0, and excitation frequency ω_0.

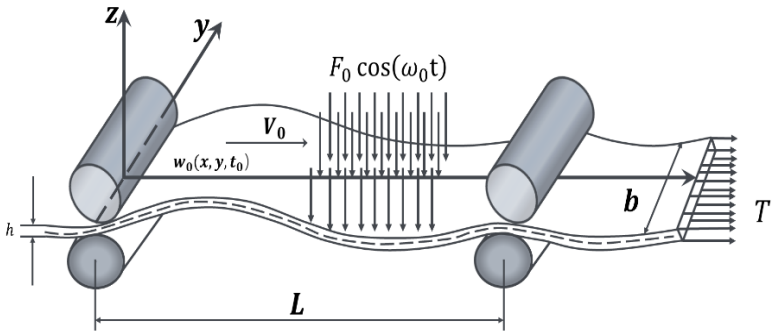

Figure 7. Schematic diagram of the axially moving belt system.

To simplify the computation, the following dimensionless parameters are introduced:

$$w = w_0/L\,, \eta = L/b\,, \varepsilon = D/TL^2\,, F = F_0/TL^2\,, t = t_0\sqrt{T/\rho AL^2}\,, V = V_0\sqrt{\rho A/T},$$
$$\omega = \omega_0\sqrt{\rho hL^2/T}\,, c = c_0\,L/\sqrt{\rho AT}. \tag{40}$$

Neglecting the displacement in the y-direction, the dimensionless equation of motion and boundary conditions of the belt are:

$$\frac{d^2w}{dt^2} + 2V\frac{dw}{dt} + (V^2-1)\frac{d^2w}{dx^2} + \varepsilon\frac{d^4w}{dx^4} + c\frac{dw}{dt} = F\,cos(\omega t),$$
$$w|_{x=0} = w|_{x=1} = 0. \tag{41}$$

Combining the boundary conditions and using the Galerkin method to separate x and t, the nonlinear equation of motion for an axially moving system can be expressed as:

$$\boldsymbol{M}\frac{d^2\boldsymbol{q}}{dt^2} + \boldsymbol{C}\frac{dq}{dt} + (\boldsymbol{K}+\boldsymbol{K}_3)\boldsymbol{q} = \boldsymbol{f}\,cos(\,\omega t). \tag{42}$$

Here, the displacement vector $\boldsymbol{q} = [q_1, q_2]^T$ represents two transverse modes. The external load vector $\boldsymbol{f}$, mass matrix $\boldsymbol{M}$, damping matrix $\boldsymbol{C}$, stiffness matrix $\boldsymbol{K}$, and nonlinear stiffness matrix $\boldsymbol{K}_3$ are given by:

$$\boldsymbol{M} = \begin{bmatrix}1 & 0\\ 0 & 1\end{bmatrix}, \boldsymbol{C} = \begin{bmatrix}c & -\frac{16}{3}V\\ \frac{16}{3}V & c\end{bmatrix}, \boldsymbol{K} = \begin{bmatrix}\omega_1^2 & 0\\ 0 & \omega_2^2\end{bmatrix},$$

$$\boldsymbol{K}_3 = \begin{bmatrix} k_{11}q_1^2 + \frac{1}{3}k_{12}q_2^2 & \frac{2}{3}k_{12}q_1q_2 \\ \frac{2}{3}k_{21}q_1q_2 & k_{22}q_2^2 + \frac{1}{3}k_{21}q_1^2 \end{bmatrix}, \boldsymbol{f} = [f_1; 0].$$

When the axial speed $V = 0.6$, the parameters in Eq (42) are $\omega_1^2 = 9.2388; \omega_2^2 = 72.02$, $c = 0.04$, $k_{11} = 4.11$, $k_{12} = 32.84$, $k_{21} = 32.84$, $k_{22} = 65.69$, $f_1 = 0.5$, all taken from [40]. At this time, the natural frequency ratio of the system satisfies $\omega_2/\omega_1 \approx 3$, and internal resonance occurs. Let $N = 5$; $\tau = \omega t$, the solution is assumed in the form:

$$q_i(\tau) = \sum_{k=1}^{N} a_{i,2k-1}\cos(2k-1)\tau + b_{i,2k-1}\sin(2k-1)\tau, i = 1,2. \tag{43}$$

Figure 8 shows the periodic responses obtained by the fourth-order RK method, the IHB method, and TRE-IHB. The time histories and phase portraits given by TRE-IHB agree with those obtained by RK and IHB, indicating that the TRE-IHB algorithm is reliable and has accuracy consistent with that of IHB.

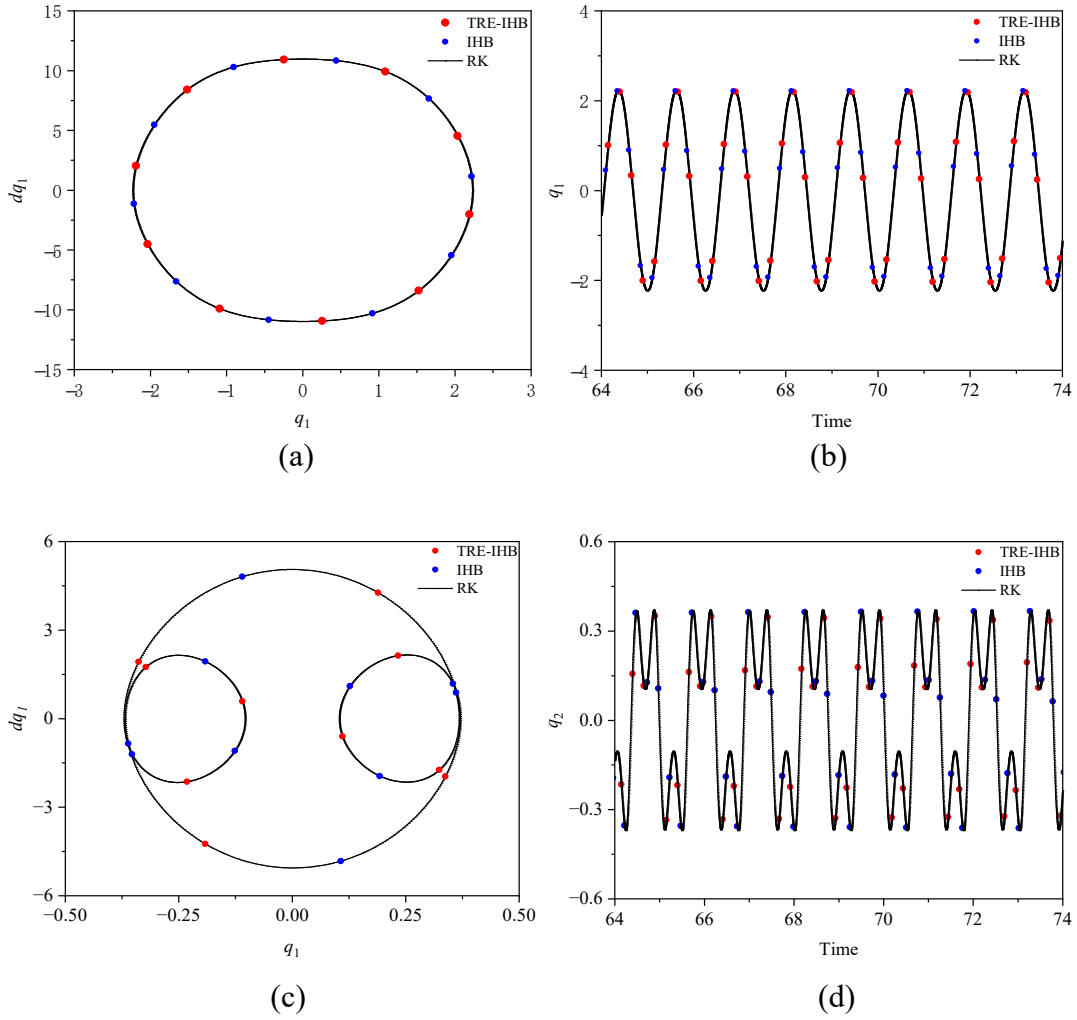

Figure 8. Periodic response of the axially moving belt/plate for $\omega = 5$: (a) phase portrait of q_1; (b) time history of q_1; (c) phase portrait of q_2; (d) time history of q_2.

To quantitatively evaluate the robustness to initial values, convergence analysis is performed over the plane spanned by the initial harmonic coefficients $a_{1,1}$ and $b_{1,1}$ (with all other coefficients set to zero), where test points are uniformly sampled in $[-10,10] \times [-10,10]$, as shown in Figure 9. The convergence points of the IHB method are highly concentrated in a narrow region with small initial residuals, exhibiting strong sensitivity to initial values. Due to the trust-region algorithm, TR-IHB shows reduced sensitivity to initial values. Building on the trust-region algorithm, the asymptotic parameter algorithm in the TRE-IHB method enables correction of the iterative path, resulting in convergence points distributed across the entire planar region.

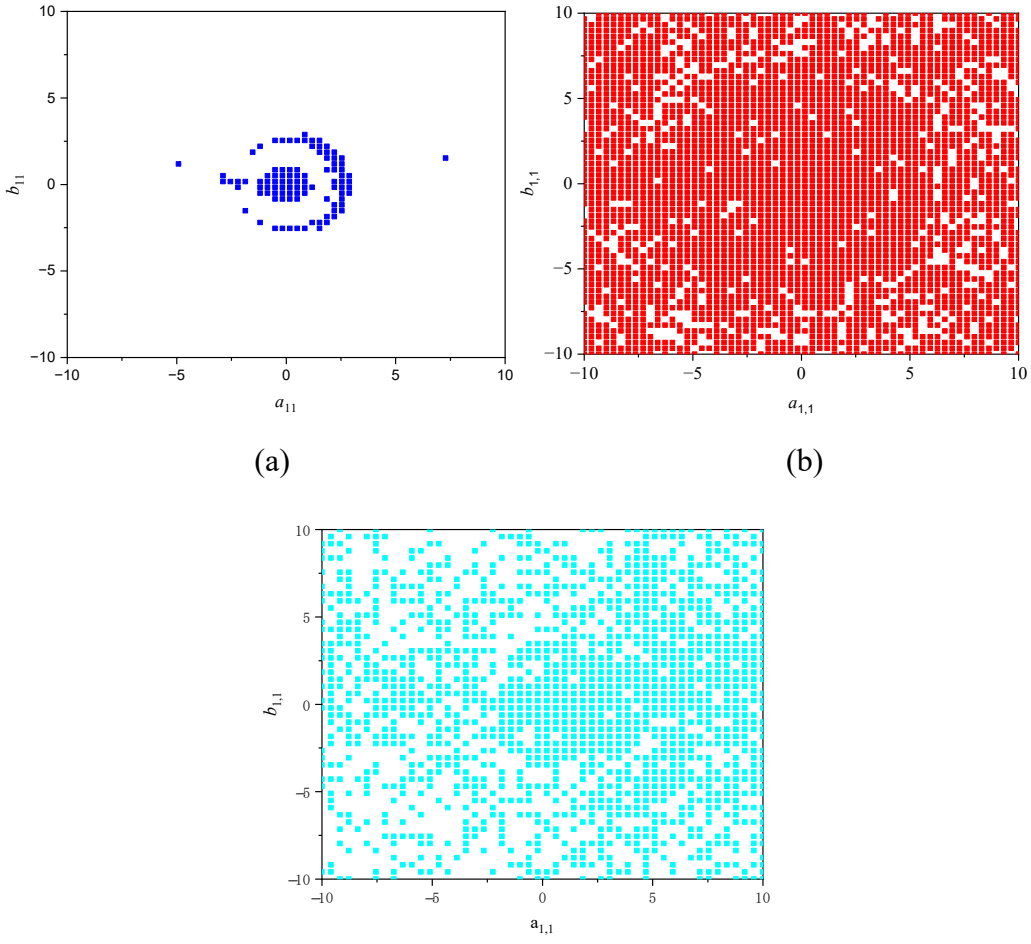

Figure 9. Basins of convergence for different initial values $(a_{1,1}, b_{1,1})$ under internal resonance: (a) IHB; (b) TRE-IHB; (c) TR-IHB.

When the initial residual is small, with initial harmonic coefficients $a_{1,1} = 2.88$ and $b_{1,1} = 0.5$, as shown in Figure 10(a), all three methods converge rapidly. Compared with the current mainstream TR-IHB (IHB with a trust-region algorithm), TRE-IHB takes longer iteration steps due to the acceleration from the asymptotic expansion. Compared with the IHB method, the residual of TRE-IHB decreases more smoothly, reflecting the stability of the serialized solution. When the initial residual is large, with initial harmonic coefficients $a_{1,1} = -10$ and $b_{1,1} = -4.4$, as shown in Figure 10(b), the IHB iterations oscillate and fail to converge [see Figure 11(a)], whereas TRE-IHB and TR-IHB achieve convergence to the physical solution after 13 and 26 iterations, respectively,

through trust-region control. It is worth noting that, if the jump–backtracking strategy is disabled, the algorithm enters a local minimum at the fifth iteration and becomes stalled, as shown in Figure 11(b), highlighting the key role of this mechanism in escaping local plateaus and ensuring global convergence.

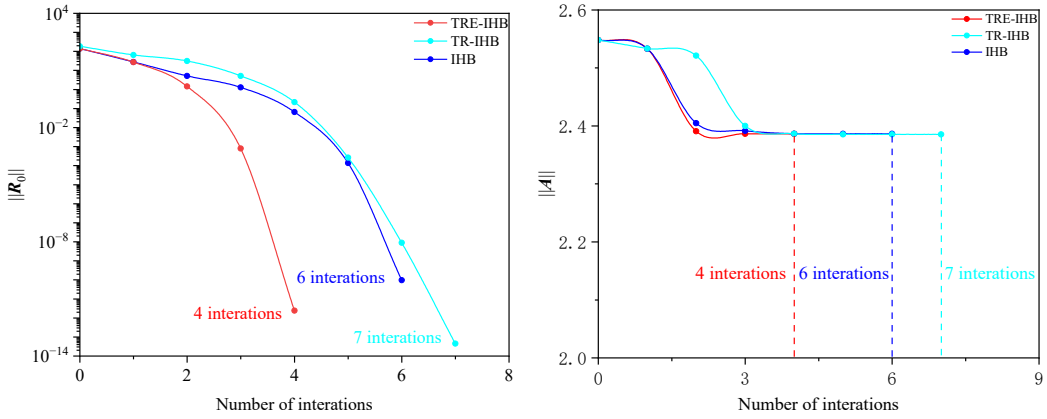

(a) (b)

Figure 10. Iteration process for the small-residual case: (a) variation of $\| \boldsymbol{R}_0 \|$ during the iterations; (b) variation of $\| \boldsymbol{A} \|$ during the iterations.

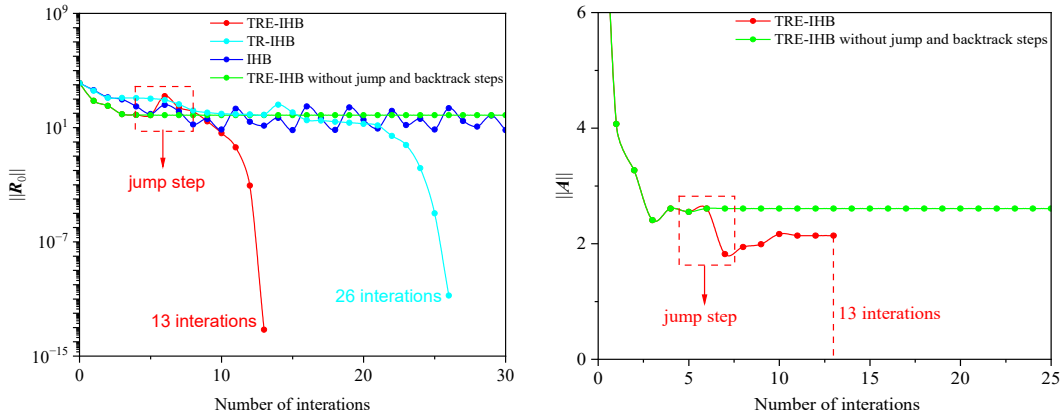

(a) (b)

Figure 11. Iteration process for the large-residual case: (a) variation of $\| \boldsymbol{R}_0 \|$ during the iterations; (b) variation of $\| \boldsymbol{A} \|$ during the iterations.

From the comparison of the frequency response curves obtained by the fourth-order RK method, the IHB method, and TRE-IHB in Figure 12, the fourth-order RK method can capture only stable solutions, whereas TRE-IHB and IHB can simultaneously reveal stable and unstable branches, providing a complete picture of the nonlinear response that includes multiple jump points such as QS_1, QS_2, and QS_3. Near jump points, IHB often maintains numerical stability by drastically reducing the step size, which leads to low efficiency and may cause distortion of the curve. In contrast, TRE-IHB smooths the solution path via asymptotic expansion and adaptively adjusts the step size through the trust-region algorithm, thereby achieving both numerical stability and computational efficiency when traversing the jump points. Specifically, the jumps at QS_1 and QS_2 mainly arise from nonlinear

hardening and bifurcation of the q_1 mode; the jump at QS_3 and the associated secondary resonance peak provide a direct manifestation of nonlinear energy transfer induced by internal resonance.

The unified framework of TRE-IHB effectively handles these complex jumps arising from different physical mechanisms. Table 2 shows that the required sampling points, iteration counts, and computing time of TRE-IHB are all only approximately 28% of those of the conventional IHB method. This indicates that TRE-IHB offers clear advantages in both robustness and efficiency for strongly nonlinear systems with multiple solution branches, abrupt jumps, and internal resonance.

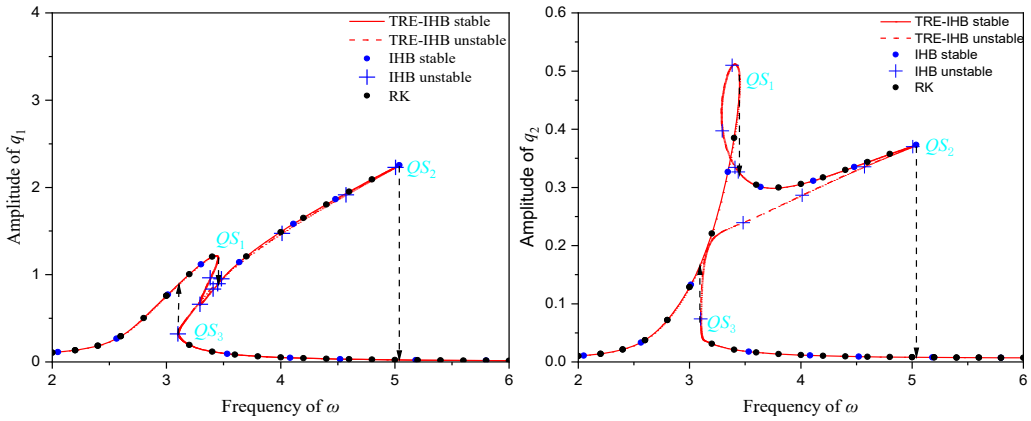

(a) (b)

Figure 12. Frequency–amplitude response curves: (a) frequency–amplitude response curve of q_1; (b) frequency–amplitude response curve of q_2.

Table 2. Related computational parameters for the frequency–amplitude response curves in Figure 12.

	Number of points	Total iterations	Total computing time (s)
IHB	503	1449	658.66
TRE-IHB	137	458	185.71

4.3. Periodic response of the Bouc–Wen hysteretic equation

The Bouc–Wen hysteretic system poses convergence difficulties and stability challenges due to the discontinuity of its governing differential equation and its strong nonlinearity. The dynamical model of the system is shown in Figure 13 [41], and its nonlinear equations are:

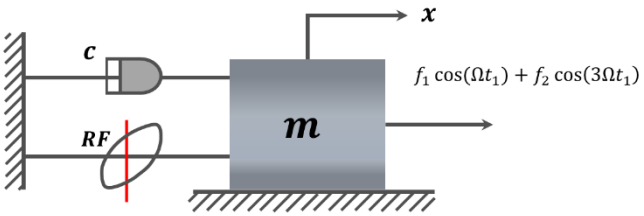

Figure 13. Bouc–Wen hysteretic model.

$$m\frac{d^2x}{dt_1^2}+c\frac{dz}{dt_1}+\alpha k_1 x+k_2 z=f_1\cos(\Omega t_1)+f_2\cos(3\Omega t_1),$$
$$\frac{dz}{dt_1}=\frac{dx}{dt_1}-\beta_1\left|\frac{dx}{dt_1}\right||z|^{n-1}z-\gamma_1\frac{dx}{dt_1}|z|^n. \tag{44}$$

For convenience in computation, introduce the characteristic frequency $\omega_0=\sqrt{\frac{k_1}{m}}$ and characteristic length L, and define the dimensionless variables as

$$q_1=\frac{x}{L},q_2=\frac{z}{L},\omega=\frac{1}{\omega_0}\Omega,\lambda=\frac{k_2}{m\omega_0^2},\xi=\frac{c}{\sqrt{k_1 m}},t=\omega_0 t_1,$$
$$F_1=\frac{f_1}{k_1 L},\ F_2=\frac{f_2}{k_1 L},\beta=\beta_1 L^n,\gamma=\gamma_1 L^n. \tag{45}$$

By rewriting Eq (44) in matrix form, the dimensionless Bouc–Wen hysteretic matrix equation is obtained as

$$\boldsymbol{M}\frac{d^2\boldsymbol{q}}{dt^2}+\boldsymbol{C}\frac{d\boldsymbol{q}}{dt}+\boldsymbol{RF}\left(\boldsymbol{q},\frac{d\boldsymbol{q}}{dt}\right)=\boldsymbol{F}, \tag{46}$$

where

$$\boldsymbol{M}=\begin{bmatrix}1&0\\0&0\end{bmatrix},\boldsymbol{C}=\begin{bmatrix}\xi&0\\-1&1\end{bmatrix},\boldsymbol{RF}\left(\boldsymbol{q},\frac{d\boldsymbol{q}}{dt}\right)=\begin{bmatrix}\alpha q_1+\lambda q_2\\ \beta\left|\frac{dq_1}{dt}\right||q_1|^{n-1}q_2+\gamma|q_2|^n\frac{dq_1}{dt}\end{bmatrix},$$
$$\boldsymbol{F}=[F_1\cos(\omega t)+F_2\cos(3\omega t);0]^T,\boldsymbol{q}=[q_1;q_2]^T.$$

The nonlinear parameters of the above Bouc–Wen model are $\beta=2,\ \gamma=8,\ n=2$. The system also includes a linear spring with stiffness $\alpha=1.667$ and a viscous damper with damping coefficient $\xi=0.1$. The parameter λ is used to adjust the restoring force contributed by q_2, with $\lambda=98.33$. The excitation amplitudes are $F_1=20,=10$, and the magnitude of the hysteretic force is $\boldsymbol{RF}(1,1)=\alpha q_1+\lambda q_2$. All of the above parameters are taken from [41]. Meanwhile, to eliminate the adverse effect of the nonsmooth absolute-value term $|q_1|$ on numerical convergence, a continuous equation is constructed for computation, i.e., where ε is a positive parameter much smaller than 1. This function is continuously differentiable over the entire domain, thereby ensuring the continuity of the TRE-IHB algorithm. Let the harmonic truncation be $N=8$. The periodic solution can be expressed as:

$$q_i(\tau)=\sum_{k=1}^{N}a_{i,2k-1}\cos(2k-1)\tau+b_{i,2k-1}\sin(2k-1)\tau,i=1,2. \tag{47}$$

For the external excitation frequency $\omega=3.06$, Figure 14 presents the periodic response of q_1 in the Bouc–Wen hysteretic model. The time histories and phase portraits obtained by TRE-IHB agree with those from RK and IHB. Two inner loops are observed in the phase portrait, indicating that TRE-IHB can handle multi-loop oscillations within one vibration period, and its accuracy is consistent with that of IHB.

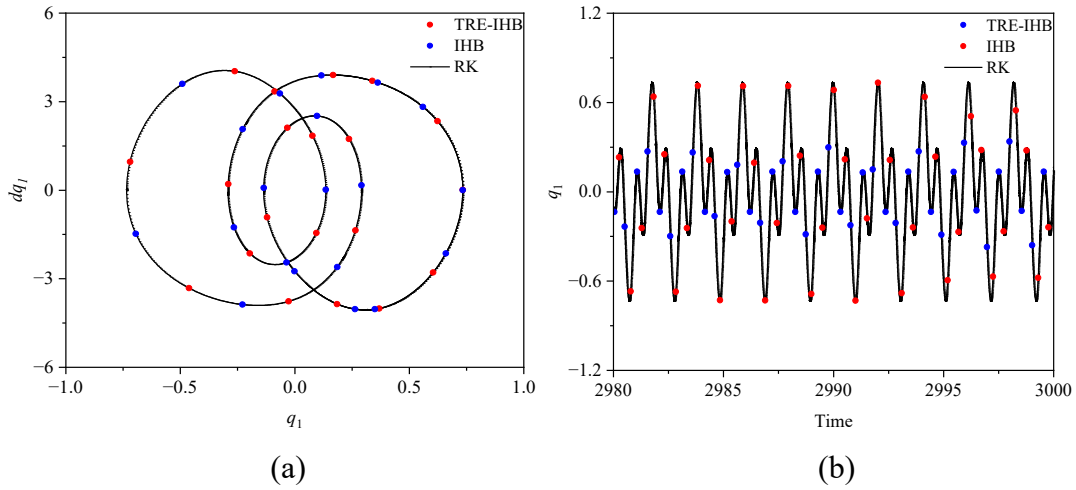

Figure 14. Periodic response of the hysteretic model at $\omega = 3.06$: (a) phase portrait of q_1; (b) time history of q_1.

The hysteresis loops and time histories of the hysteretic force in Figure 15 correspond to the steady-state response shown in Figure 14. The two sawtooth-like curves in Figure 15 correspond to the two small inner loops in Figure 14(a). Due to the multi-loop response, within one period, the hysteretic force can be clearly observed to undergo multiple loading–unloading processes, as shown in Figure 15(b), which is consistent with the energy dissipation characteristic of hysteresis loops. Comparison with the fourth-order RK method and the IIHB method again verifies the accuracy of TRE-IHB.

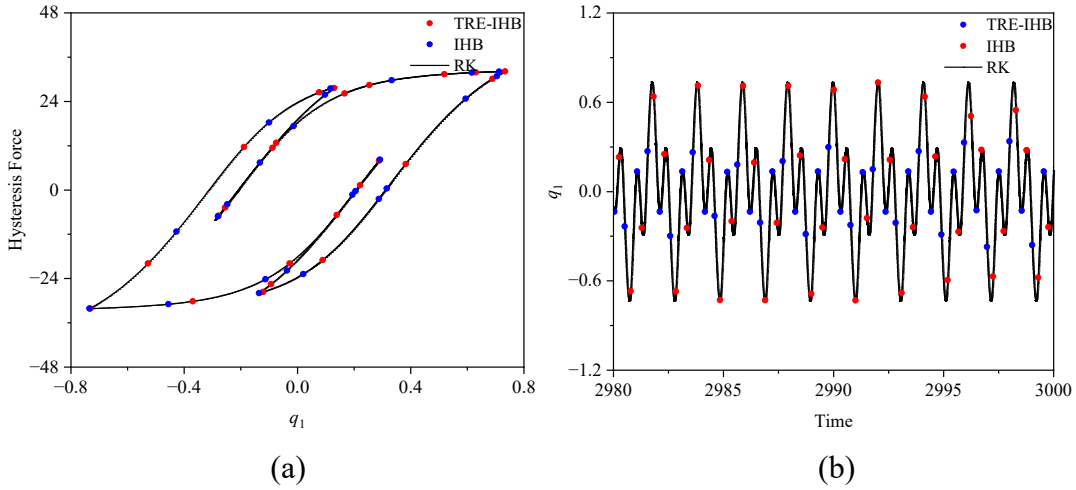

Figure 15. Hysteresis curves of the Bouc–Wen model at $\omega = 3.06$: (a) hysteresis loops; (b) time histories.

To evaluate the robustness of the algorithm with respect to the initial guess, basin-of-convergence tests are conducted over the plane spanned by the initial harmonic coefficients $a_{1,1}$ and $a_{2,1}$ (with all other coefficients set to zero). As shown in Figure 16, the convergence points of IHB are relatively scattered and mainly symmetrically distributed around the diagonal region. Compared with TR-IHB,

the convergence points of TRE-IHB cover almost the entire test region due to the correction of the iterative path by the asymptotic parameter algorithm. This indicates that the proposed method significantly broadens the basin of convergence.

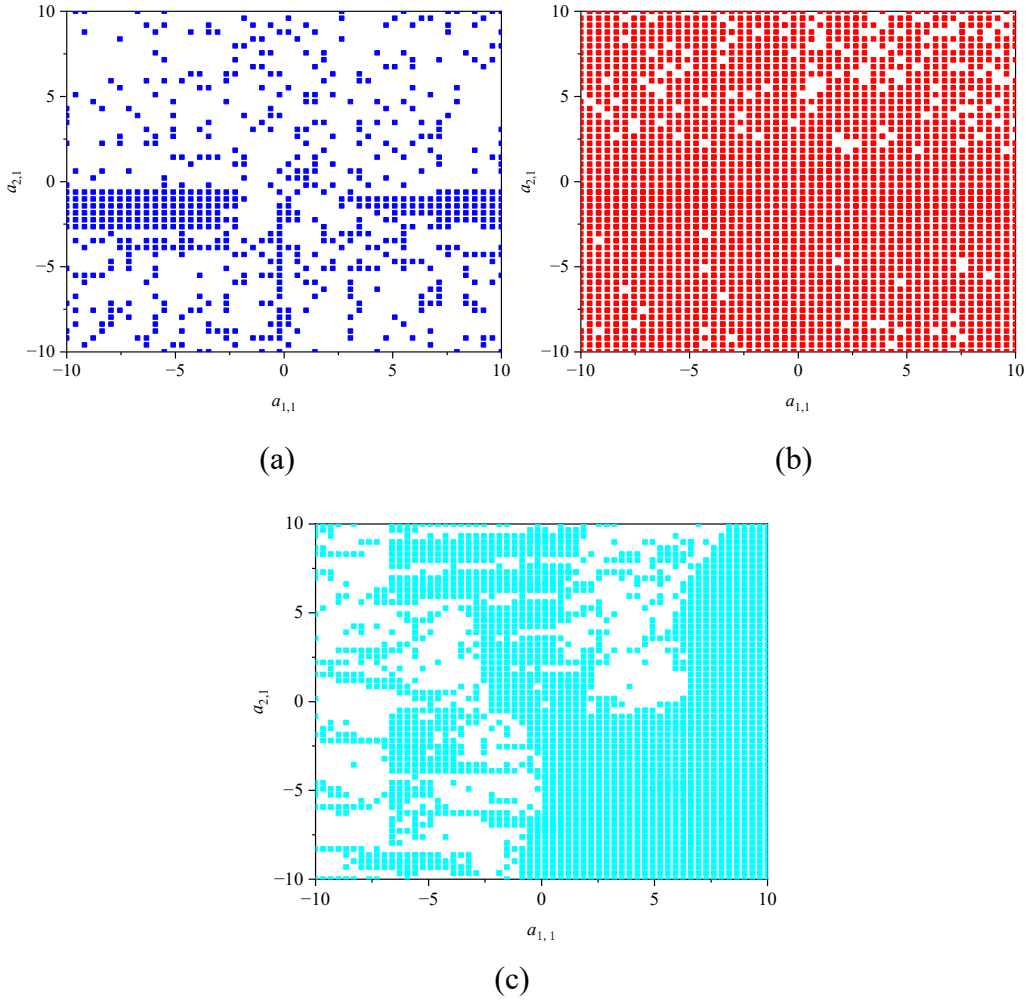

Figure 16. Basin of convergence of the Bouc–Wen model at $\omega = 3.06$: (a) IHB; (b) TRE-IHB; (c) TR-IHB.

As shown in Figure 17, when TRE-IHB, TR-IHB, and IHB all converge, the residual decay curve of TRE-IHB is smoother and more stable and requires fewer iteration steps than TR-IHB, without the slight oscillations observed in IHB during the iterations. This is attributed to the asymptotic expansion, which smooths the iteration trajectory and accelerates convergence, enabling the algorithm to approach the solution more robustly at each update. Figure 18 corresponds to the case where the initial value is far from the exact solution. Under this initial value, IHB exhibits persistent oscillations and fails to converge. In contrast, TRE-IHB, by means of asymptotic expansion, effectively corrects the iterative path within a single iteration step. Compared with TR-IHB, it reduces the number of convergence steps by 30%, as shown in Figure 18(a). For TRE-IHB, stagnation occurs in the mid-iteration stage (around the 5th and 9th iterations), where the residual reduction becomes flat. When the jump–backtracking strategy is not activated, the system cannot converge, and the error remains constant, as shown in Figure 18(b). When the jump–backtracking strategy is activated, the algorithm first performs a jump step, expanding the exploration range along the gradient direction while shrinking the trust-region

radius; then, when the second stagnation occurs, it performs a backtracking step, returning to the initial iterate $\boldsymbol{A}_0$ and following a different iteration path by further reducing the trust-region radius. These two strategic adjustments allow the algorithm to quickly escape the local plateau and restore steady descent in the subsequent iterations by reducing the trust-region radius, ultimately converging in fewer iterations.

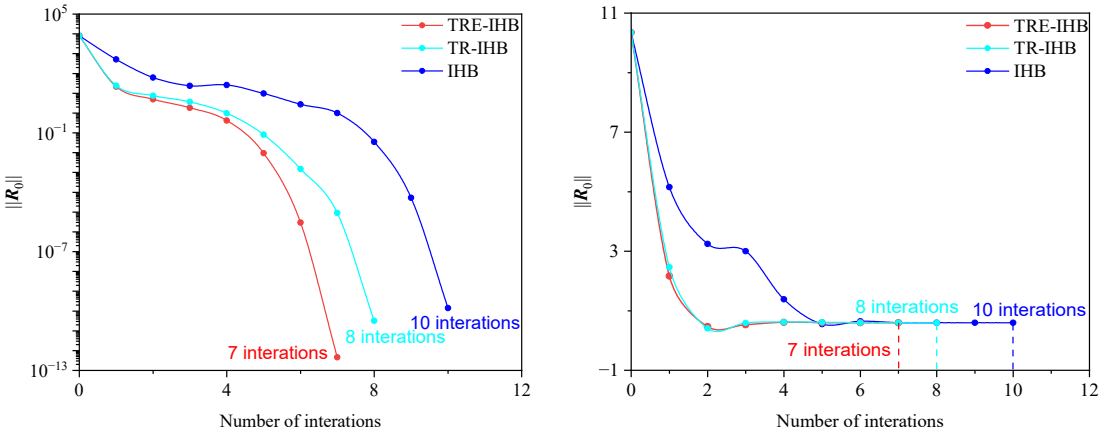

Figure 17. Iteration process with the jump–backtracking strategy not activated: (a) variation of $\| \boldsymbol{R}_0 \|$ during the iterations; (b) variation of $\|\boldsymbol{A}\|$ during the iterations.

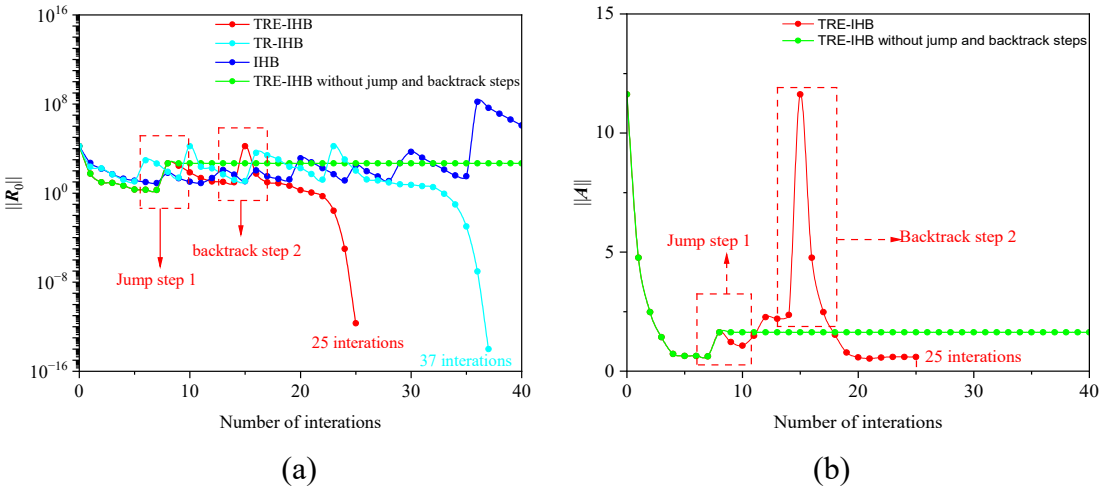

Figure 18. Iteration process with the jump–backtracking strategy activated: (a) variation of $\| \boldsymbol{R}_0 \|$ during the iterations; (b) variation of $\|\boldsymbol{A}\|$ during the iterations.

The above examples show that TRE-IHB achieves serialization of the nonlinear problem through asymptotic expansion, adaptively controls the iteration step size through the trust-region mechanism, and performs exploration and recovery under stagnation via the jump–backtracking strategy. These features effectively overcome the drawbacks of conventional IHB when dealing with nonlinear systems, including a narrow basin of convergence, sensitivity to initial guesses, and susceptibility to local plateaus, while markedly improving robustness and efficiency without sacrificing computational accuracy.

5. Conclusions

To overcome the inherent drawbacks of the conventional incremental harmonic balance (IHB) method in the analysis of strongly nonlinear systems, including a narrow basin of convergence and high sensitivity to the initial guess, this paper proposes an improved method that integrates asymptotic expansion with a trust region strategy (TRE IHB). The method introduces an asymptotic parameter and, based on the stacked Hessian matrix, decomposes the nonlinear incremental equation system into a sequence of linear subproblems, thereby achieving order-by-order decoupling. Meanwhile, a trust region algorithm is used as the inner solver to ensure global convergence of the iterations. The method is validated using three representative examples, namely the Van der Pol–Mathieu equation for parametric resonance, an axially moving belt or plate for internal resonance, and a Bouc–Wen hysteretic system. The results indicate that the proposed method has the following characteristics:

(1) Markedly improved convergence robustness. TRE-IHB substantially broadens the basin of convergence and reduces dependence on the initial guess. In regions with large residuals or near the spurious zero solution where the conventional IHB method tends to fail, the proposed method can still converge robustly to physically meaningful solutions.

(2) High efficiency without loss of accuracy. Through a serialized solution and an improved iteration path, TRE-IHB achieves the same accuracy in computing frequency response curves with fewer sampling points and fewer total iterations, and the computing time is significantly lower than that of the conventional IHB method.

(3) An effective mechanism for escaping stagnation. To address the tendency of iterations to stall in strongly nonlinear analyses, the proposed jump–backtracking strategy can adaptively identify stagnation and guide the iterate to escape local basins, thereby markedly enhancing the stability and success rate in tracking complex response curves.

(4) Good generality and portability. The core procedure of the method can be implemented in a modular and programmable manner, which facilitates convenient transfer and application to the analysis of various nonlinear vibration systems and provides practical engineering value.

Although the proposed TRE-IHB method offers the above advantages, it still has certain limitations. First, the choice of the asymptotic expansion order M remains empirical: an excessively high order increases computational cost without proportional gains in accuracy, while a low order may compromise convergence. Second, the current framework is primarily designed for periodic responses, and its extension to quasi-periodic or chaotic motions requires further investigation. Future work will focus on the following three aspects: (1) developing an adaptive strategy for selecting the expansion order to balance efficiency and accuracy; (2) extending the method to quasi-periodic responses using multi-timescale formulations; and (3) integrating model reduction techniques to improve scalability for high-degree-of-freedom systems. These efforts will further broaden the applicability of the TRE-IHB method and enhance its capability for analyzing complex dynamical systems.

Author contributions

Wentao Zhou: Writing-original draft, software, and formal analysis. Zeliang Liu: Methodology and resources. Huijian Li: Conceptualization. All authors agree to take responsibility for the content and conclusions of the manuscript.

Use of Generative-AI tools declaration

The authors declare they have not used Artificial Intelligence (AI) tools in the creation of this article.

Conflict of interest

The authors declare that they have no known competing financial interests or personal relationships that could have appeared to influence the work reported in this paper.

References

1. J. Liu, F. Wang, Y. Yang, Study of nonlinear aerodynamic self-excited force in flutter bifurcation and limit cycle oscillation of long-span suspension bridge, *Appl. Sci.*, **13** (2023), 10272. https://doi.org/10.3390/app131810272
2. H. Zhang, E. Wang, F. Min, N. Zhang, C. Su, S. Rakheja, Nonlinear dynamics analysis of the semiactive suspension system with magneto-rheological damper, *Shock Vib.*, **2015** (2015), 971731. https://doi.org/10.1155/2015/971731
3. B. Patel, P. Kundu, S. Chatterjee, Nonlinear feedback anti-control of limit cycle and chaos in a mechanical oscillator: Theory and experiment, *Nonlinear Dyn.*, **104** (2021), 3223–3246. https://doi.org/10.1007/s11071-021-06493-1
4. C. S. Liu, Y. W. Chen, A simplified Lindstedt-Poincare method for saving computational cost to determine higher order nonlinear free vibrations, *Mathematics*, **9** (2021), 3070. https://doi.org/10.3390/math9233070
5. P. Amore, A. Aranda, Improved Lindstedt-Poincare method for the solution of nonlinear problems, *J. Sound Vib.*, **283** (2005), 1115–1136. https://doi.org/10.1016/j.jsv.2004.06.009
6. A. Chakib, A. Hadri, A. Nachaoui, M. Nachaoui, Multiscale computational method for nonlinear heat transmission problem in periodic porous media, *Appl. Numer. Math.*, **150** (2020), 164–181. https://doi.org/10.1016/j.apnum.2019.09.015
7. H. Li, S. Wang, S. Liu, Z. Deng, J. Xu, Lateral-vertical coupled nonlinear vibration characteristics of HTS maglev based on multiscale method and experimental test, *Mech. Syst. Signal Process.*, **240** (2025), 113449. https://doi.org/10.1016/j.ymssp.2025.113449
8. G. Ge, Z. Li, Q. Gao, J. Duan, A stochastic averaging method on the strongly nonlinear Duffing-Rayleigh oscillator under Gaussian colored noise excitation, *J. Vibroeng.*, **18** (2016), 4766–4775. https://doi.org/10.21595/jve.2016.17011
9. G. Ge, N. Xie, An approach dealing with inertia nonlinearity of a cantilever model subject to lateral basal Gaussian white noise excitation, *Chaos Soliton Fract.*, **131** (2020), 109469. https://doi.org/10.1016/j.chaos.2019.109469
10. M. Cai, W. F. Liu, J. K. Liu, Bifurcation and chaos of airfoil with multiple strong nonlinearities, *Appl. Numer. Math.*, **34** (2013), 627–636. https://doi.org/10.1007/s10483-013-1696-x
11. T. Tuloup, R. W. Bomantara, J. Gong, Breakdown of quantization in nonlinear Thouless pumping, *New J. Phys.*, **25** (2023), 083048. https://doi.org/10.1088/1367-2630/acef4d
12. R. Kruse, Optimal error estimates of Galerkin finite element methods for stochastic partial differential equations with multiplicative noise, *IMA J. Numer. Anal.*, **34** (2014), 217–251. https://doi.org/10.1093/imanum/drs055

13. J. Li, B. Wang, A finite element method for nonlinear and fully coupled transient hygrothermal transfer, *Appl. Sci.*, **15** (2025), 7372. https://doi.org/10.3390/app15137372
14. Z. Liu, Y. Qiao, X. Cheng, Z. Huang, IBEM-FEM coupling method for full process nonlinear ground motion simulation of near-fault sedimentary basins, *Soil Dyn. Earthq. Eng.*, **170** (2023), 107916. https://doi.org/10.1016/j.soildyn.2023.107916
15. V. P. Iu, Y. K. Cheung, S. L. Lau, Non-linear vibration analysis of multilayer besams by incremental finite elements, Part I: Theory and numerical formulation, *J. Sound Vib.*, **100** (1985), 359–372. https://doi.org/10.1016/0022-460X(85)90292-5
16. J. L. Huang, B. X. Zhang, W. D. Zhu, Quasi-periodic solutions of a damped nonlinear quasi-periodic mathieu equation by the incremental harmonic balance method with two time scales, *J. Appl. Mech.*, **89** (2022), 091009. https://doi.org/10.1115/1.4055086
17. A. Hadji, N. Mureithi, Validation of friction model parameters identified using the IHB method using finite element method, *Shock Vib.*, **2019** (2019), 3493052. https://doi.org/10.1155/2019/3493052
18. Z. Chang, L. Hou, R. Lin, Y. Jin, Y. Chen, A modified IHB method for nonlinear dynamic and thermal coupling analysis of rotor-bearing systems, *Mech. Syst. Signal Process.*, **200** (2023), 110586. https://doi.org/10.1016/j.ymssp.2023.110586
19. Y. Cong, S. Jin, H. Kang, Dynamic analysis of a double-cable-stayed shallow arch model under multi-frequency excitation by IHB method, *Int. J. Struct. Stab. Dyn.*, **25** (2025), 2550033. https://doi.org/10.1142/S0219455425500336
20. X. Wu, R. Zhong, R. Wang, Q. Wang, A Chebyshev-IHB solution for nonlinear vibrations of laminated circular plates, *Nonlinear Dyn.*, **113** (2025), 25787–25800. https://doi.org/10.1007/s11071-025-11440-5
21. Z. Li, S. Zhou, H. Zhang, S. Zhou, Periodic solutions and bifurcations of a tristable flutter-based energy harvester, *Aerosp. Sci. Technol.*, **144** (2024), 108815. https://doi.org/10.1016/j.ast.2023.108815
22. Q. Wu, Y. Wang, D. Cao, Nonlinear dynamic analysis of high aspect ratio wings via IHB method, *Nonlinear Dyn.*, **113** (2025), 16225–16244. https://doi.org/10.1007/s11071-025-10975-x
23. W. Lu, F. Ge, X. Wu, Y. Hong, Nonlinear dynamics of a submerged floating moored structure by incremental harmonic balance method with FFT, *Mar. Struct.*, **31** (2013), 63–81. https://doi.org/10.1016/j.marstruc.2013.01.002
24. X. F. Wang, W. D. Zhu, A modified incremental harmonic balance method based on the fast Fourier transform and Broyden's method, *Nonlinear Dyn.*, **81** (2015), 981–989. https://doi.org/10.1007/s11071-015-2045-x
25. R. Ju, W. Fan, W. Zhu, An efficient Galerkin averaging-incremental harmonic balance method based on the fast fourier transform and tensor contraction, *J. Vib. Acoust.*, **142** (2020), 061011. https://doi.org/10.1115/1.4047235
26. Y. Hui, S. S. Law, W. Zhu, Efficient algorithm for the dynamic analysis of large civil structures with a small number of nonlinear components, *Mech. Syst. Signal Process.*, **152** (2021), 107480. https://doi.org/10.1016/j.ymssp.2020.107480
27. Y. Chen, Y. Jin, R. Lin, Y. Jiang, X. Mei, L. Hou, et al., Harmonic balance-automatic differentiation method: A practical nonlinear dynamics solver, *Int. J. Mech. Sci.*, **312** (2026), 111192. https://doi.org/10.1016/j.ijmecsci.2026.111192

28. Y. Chen, L. Hou, R. Lin, J. Song, T. Ng, Y. Chen, A harmonic balance method combined with dimension reduction and FFT for nonlinear dynamic simulation, *Mech. Syst. Signal Process.*, **223** (2025), 111848. https://doi.org/10.1016/j.ymssp.2024.111848
29. Y. Chen, J. Liu, Improving convergence of incremental harmonic balance method using homotopy analysis method, *Acta Mech. Sin.*, **25** (2009), 707–712. https://doi.org/10.1007/s10409-009-0256-4
30. Z. C. Zheng, Z. R. Lu, Y. M. Chen, J. K. Liu, G. Liu, A modified incremental harmonic balance method combined with tikhonov regularization for periodic motion of nonlinear system, *J. Appl. Mech.*, **89** (2022), 021001. https://doi.org/10.1115/1.4052573
31. Y. L. Li, J. L. Huang, W. D. Zhu, An enhanced incremental harmonic balance method to improve the computational efficiency and convergence for systems with non-polynomial nonlinearities, *Nonlinear Dyn.*, **113** (2025), 8265–8294. https://doi.org/10.1007/s11071-024-10739-z
32. H. Dai, Z. Yan, X. Wang, X. Yue, S. Atluri, Collocation-based harmonic balance framework for highly accurate periodic solution of nonlinear dynamical system, *Int. J. Numer. Methods Eng.*, **124** (2023), 458–481. https://doi.org/10.1002/nme.7128
33. H. Dai, Q. Wang, Z. Yan, X. Yue, Reconstruction harmonic balance method and its application in solving complex nonlinear dynamical systems, *Chin. J. Theor. Appl. Mech.*, **56** (2024), 212–224. https://doi.org/10.6052/0459-1879-23-369
34. P. Wu, J. Wang, C. Mao, Y. Zhao, Nonlinear random vibration analysis of bolted composite structure considering hysteresis effect, *J. Vib. Shock*, **43** (2024), 223–230.
35. J. Huang, B. Zhang, S. Chen, Two generalized incremental harmonic balance methods with optimization for iteration step, *Chin. J. Theor. Appl. Mech.*, **54** (2022), 1353–1363. https://doi.org/10.6052/0459-1879-22-042
36. S. Dou, An improved tensorial implementation of the incremental harmonic balance method for frequency-domain stability analysis, In: *Advances in nonlinear dynamics*, 2022, 443–452.
37. M. Xu, Q. Zhu, H. Xiao, An improved non-monotonic adaptive trust region algorithm for unconstrained optimization, *Mathematics*, **12** (2024), 3398. https://doi.org/10.3390/math12213398
38. Y. Dong, Z. Wang, X. Mao, M. Amabili, On the combined iteration scheme of harmonic balance-pseudo arclength-extrapolation method applied to the nonlinear systems with nonlinear damping and time delay, *Nonlinear Dyn.*, **113** (2025), 20729–20746. https://doi.org/10.1007/s11071-025-11284-z
39. J. Huang, T. Wang, W. Zhu, An incremental harmonic balance method with two time-scales for quasi-periodic responses of a Van der Pol-Mathieu equation, *Int. J. Non-Linear Mech.*, **135** (2021), 103767. https://doi.org/10.1016/j.ijnonlinmec.2021.103767
40. M. Ghayesh, M. Amabili, M. Païdoussis, Nonlinear dynamics of axially moving plates, *J. Sound Vib.*, **332** (2013), 391–406. https://doi.org/10.1016/j.jsv.2012.08.013
41. Y. Hui, S. S. Law, W. Zhu, Q. Yang, Extended IHB method for dynamic analysis of structures with geometrical and material nonlinearities, *Eng. Struct.*, **205** (2020), 110084. https://doi.org/10.1016/j.engstruct.2019.110084